

Real-Time Oriented Object Detection Transformer in Remote Sensing Images

Zeyu Ding[✉], Yong Zhou[✉], Jiaqi Zhao[✉], *Member, IEEE*, Wen-Liang Du[✉] *Member, IEEE*, Xixi Li *Member, IEEE*, Rui Yao[✉], *Member, IEEE*, and Abdulmotaleb El Saddik[✉], *Fellow, IEEE*

Abstract—Recent real-time detection transformers have gained popularity due to their simplicity and efficiency. However, these detectors do not explicitly model object rotation, especially in remote sensing imagery where objects appear at arbitrary angles, leading to challenges in angle representation, matching cost, and training stability. In this paper, we propose a real-time oriented object detection transformer, the first real-time end-to-end oriented object detector to the best of our knowledge, that addresses the above issues. Specifically, angle distribution refinement is proposed to reformulate angle regression as an iterative refinement of probability distributions, thereby capturing the uncertainty of object rotation and providing a more fine-grained angle representation. Then, we incorporate a Chamfer distance cost into bipartite matching, measuring box distance via vertex sets, enabling more accurate geometric alignment and eliminating ambiguous matches. Moreover, we propose oriented contrastive denoising to stabilize training and analyze four noise modes. We observe that a ground truth can be assigned to different index queries across different decoder layers, and analyze this issue using the proposed instability metric. We design a series of model variants and experiments to validate the proposed method. Notably, our O²-DFINE-L, O²-RTDETR-R50 and O²-DEIM-R50 achieve 77.73%/78.45%/80.15% AP₅₀ on DOTA1.0 and 132/119/119 FPS on the 🖥️ 2080ti GPU. Code is available at 🌐 <https://github.com/wokaikaixinxin/ai4rs>.

Index Terms—Oriented object detection, detection transformer, real-time detector, remote sensing.

I. INTRODUCTION

Oriented object detection [1] in remote sensing images aims to classify objects into categories and localize them using rotated boxes aligned with their arbitrary orientations. Remote sensing applications typically require real-time detection with low latency. Existing real-time oriented object detection methods are primarily based on CNN models, with many adopting the YOLO framework [2]–[4] due to its reasonable trade-off between speed and accuracy. These approaches typically extend standard YOLO detectors by adding angle prediction branches to support rotated outputs. However, these models

Received 27 December 2025; revised 23 February 2026; accepted 3 March 2026.

Zeyu Ding, Yong Zhou, Jiaqi Zhao, Wen-Liang Du, Xixi Li, and Rui Yao are with the School of Computer Science and Technology / School of Artificial Intelligence, China University of Mining and Technology, Xuzhou 221116, China, and with the Mine Digitization Engineering Research Center of the Ministry of Education, Xuzhou 221116, China, and also with the Jiangsu Provincial Industrial Technology Engineering Center for Intelligent Sensing and Emergency IoT in Underground Space, Xuzhou 221116, China (e-mails: {dingzeyu, yzhou, jiaqizhao, wldu, xixili, ruiyao}@cumt.edu.cn).

Abdulmotaleb El Saddik is with the School of Electrical Engineering and Computer Science, University of Ottawa, Ottawa, ON K1N 6N5, Canada (e-mail: elsaddik@uottawa.ca).

Digital Object Identifier 10.1109/TGRS.2026.3671683

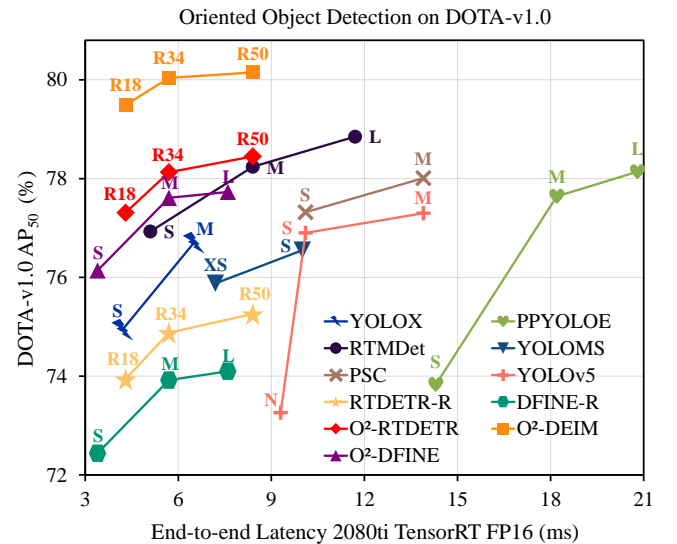


Fig. 1. Compared to existing real-time object detectors, the family of O²-DFINE, O²-RTDETR, and O²-DEIM achieves competitive performance.

rely on post-processing steps such as rotated Non-Maximum Suppression (NMS) [5], which increases latency and introduces additional parameters, as shown in Fig. 1. Furthermore, in oriented object detection, the rotated NMS process requires a rotated IoU threshold, and the results are influenced by this threshold since oriented boxes are sensitive to IoU variations.

In recent years, end-to-end detection transformer (DETR) methods [6] have gained wide attention in object detection due to their simple framework and the ability to remove hand-crafted components. DETR methods have been developed for oriented object detection, tackling challenges such as oriented object representation [7], attention mechanism design [8], query formulation [9], and label assignment [10]. However, the high computational cost often hinders their real-time performance, making them less suitable for real-time applications.

RT-DETR [11] emerged as the first real-time end-to-end detection transformer, achieving both efficiency and accuracy through a hybrid design and query selection mechanism. Following this pioneering work, several improved real-time Transformer-based detectors have been developed [12], [13]. More recently, D-FINE [14] refines the regression process by modeling boxes as fine-grained distributions, enabling more precise localization. Methods like DEIM [15] accelerate convergence through improved matching strategies. However, existing real-time detection transformers are primarily designed

for horizontal object detection in natural scenes. They lack explicit support for oriented objects, which are common in remote sensing imagery.

Objects often appear at arbitrary orientations in remote sensing images, introducing geometric rotation transformations that pose several key challenges for real-time end-to-end detection transformers. ① **Angle representation.** Most detectors predict angles by regressing a radian value, treating rotation as a precise value modeled by a Dirac delta distribution [2]. This approach fails to capture the uncertainty in object rotation. Consequently, models rely on L1 or rotated IoU losses, which offer limited supervision for fine-grained angle adjustment. This makes optimization sensitive to minor angular errors and hinders convergence. While techniques such as DFL [3] utilize distributions to represent uncertainty, they are still constrained by coarse localization and anchor dependency. ② **Matching cost.** Conventional distance metrics often introduce geometric ambiguity during bipartite matching. For instance, L1 distance may assign a lower cost to a spatially distant prediction that happens to share the same orientation, while penalizing a well-aligned but slightly rotated box. Similarly, KL divergence [16] fails to distinguish between square boxes with identical shape and center, and Hausdorff distance [10] is overly sensitive to outliers. ③ **Training stability.** We observe that a single ground-truth object can be matched to different index predicted queries across decoder layers during early training stages. The instability of bipartite graph matching causes inconsistent optimization goals. Hungarian matching exhibits unstable assignment due to the existence of blocking pairs [17]. A slight change in the cost may cause a significant change in the matching result.

To address these issues, we propose a real-time end-to-end oriented object detection transformer for remote sensing images that introduces three key innovations for the challenges of angle representation, matching cost, and training stability. **First**, we design **Angle Distribution Refinement**, which replaces direct angle regression with an iterative refinement of probability distributions, enabling the model to capture angular uncertainty and perform progressively finer residual adjustments in a residual manner. **Second**, we incorporate **Chamfer Distance Cost** into bipartite matching by measuring the distance between oriented boxes via their vertices, which alleviates ambiguous matches caused by traditional distance costs and ensures that only spatially and rotationally aligned predictions are favored. **Third**, we introduce **Oriented Contrastive Denoising**, a training strategy that injects noise into oriented boxes to generate positive and negative query pairs across four modes. We propose an instability metric to verify that this mechanism stabilizes label assignment. We develop a family of detectors and perform extensive experiments on four datasets. Our O²-DFINE-L, O²-RTDETR-R50, and O²-DEIM-R50 achieve 77.73%/78.45%/80.15% AP₅₀ on DOTA1.0 and 132/119/119 FPS on the 2080ti GPU.

The contributions of this work are summarized as follows:

- 1) To model the uncertainty in object rotation angles, we introduce Angle Distribution Refinement, which provides a fine-grained representation and enables progressively finer adjustments.

- 2) To alleviate ambiguous matches caused by suboptimal distance costs, we incorporate the Chamfer Distance Cost into bipartite matching, enabling more accurate geometric alignment.
- 3) To mitigate training instability in label assignment, we propose Oriented Contrastive Denoising with four noise injection modes. We further introduce an instability metric to verify its effectiveness.
- 4) As far as we know, our method is the first real-time oriented object detection transformer, with variants including O²-RTDETR, O²-DFINE, and O²-DEIM. Experiments demonstrate that the method achieves competitive performance with real-time inference speed.

II. RELATED WORK

A. Oriented Object Detection in Remote Sensing

Oriented object detection in remote sensing imagery aims to localize objects with arbitrary orientations. Existing methods can be broadly categorized into CNN-based, transformer-based, and random-initialization approaches according to how object candidates are generated. CNN-based methods include both two-stage [1], [18] and single-stage [19], [20] detectors. Two-stage methods generate region proposals that are subsequently refined, while single-stage methods directly predict object classes and oriented bounding boxes from densely placed anchors in a single forward pass. Transformer-based methods formulate oriented object detection as a set prediction problem using a fixed number of learnable queries [7], [8]. These methods directly predict oriented bounding boxes in an end-to-end manner, eliminating the need for anchors or proposal generation. Random-initialization methods represent object candidates using randomly initialized primitives. These methods refine Gaussians into oriented boxes through Gaussian splatting [21] or denoising diffusion [22], and typically support a dynamic number of candidates and enable flexible inference.

In contrast to existing CNN-based [23]–[27] and random-initialization methods, our approach is fully end-to-end and avoids handcrafted post-processing such as non-maximum suppression. Compared with prior transformer-based detectors, our method further achieves real-time inference.

B. Detection Transformer in Oriented Object Detection

Existing detection transformers for oriented object detection can be broadly categorized by their core technical designs, including oriented object representation, rotation-aware attention, query formulation, and label assignment. Some works focus on oriented object representations to mitigate angle ambiguity, such as point-based [7] or oriented-box-based [28] query formulations, or decoupled angle modeling to reduce error propagation [29]. Another line of research enhances attention mechanisms with rotation awareness, for example, by rotating sampling locations [8], introducing rotation-equivariant feature extraction [28], or designing geometry-aware self- and cross-attention modules [30] to better capture oriented object structures. Query design has also been explored to improve efficiency and suppress redundancy,

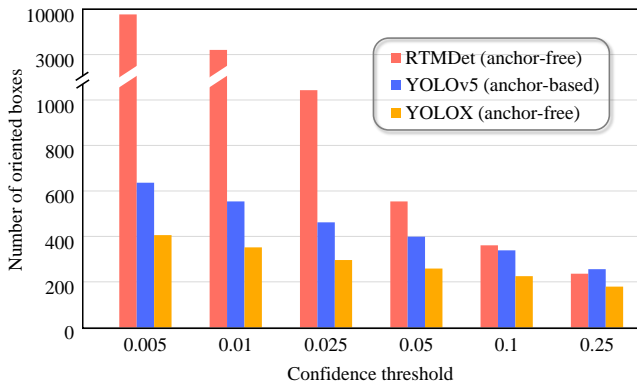


Fig. 2. The number of remaining oriented boxes above different confidence thresholds in rotated NMS.

TABLE I
EFFECT OF ROTATED IOU THRESHOLDS AND CONFIDENCE THRESHOLDS ON RTMDet-S ACCURACY FOR DOTA-V1.0.

RIoU thr. (Conf=0.05)	Conf thr.			RIoU thr. (RIoU=0.1)	Conf thr.		
	0.05	0.3	0.5		0.01	0.05	0.25
AP ₅₀ (%)	76.53	76.72	76.70	AP ₅₀ (%)	76.82	76.86	75.61

including representing objects as point sets, generating selective distinct queries [9], and encouraging query diversity during training [29]. Label assignment strategies are further adapted to aerial imagery, addressing unbalanced object distributions and redundant predictions through dynamic matching schemes [28], geometry-aware matching costs [10], or high-quality sample selection [31].

In contrast to these methods, our method represents the first real-time detection transformer for oriented object detection.

C. Real-time Object Detectors

Real-time object detection has remained a key focus area within computer vision. Among the most influential frameworks in this area is the YOLO series [32]. Early YOLO models established the one-stage detection paradigm for fast inference, while later variants improved the speed-accuracy trade-off through enhanced multi-scale feature representations [33], decoupled detection heads [34], efficient backbones [35], and attention modules [36].

Despite their efficiency, most YOLO-based detectors rely on NMS to remove duplicate predictions, which introduces additional latency and may lead to unstable results in dense scenes, such as remote sensing imagery. This limitation has motivated the development of end-to-end real-time detectors. RT-DETR [11] emerged as the first end-to-end real-time detection transformer by introducing efficient encoder design and query selection. Subsequent works further improved localization accuracy and training efficiency by refining regression representations and enhancing matching-based supervision [14], [15].

Unlike existing real-time detection transformers, our method explicitly supports oriented object detection and robustly handles arbitrarily rotated objects commonly found in remote sensing imagery.

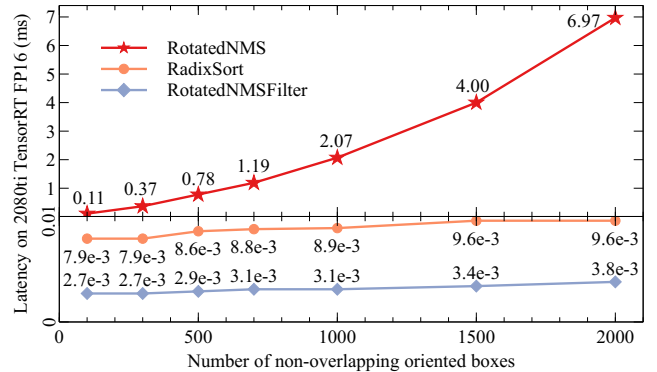


Fig. 3. Execution time of rotated NMS with different numbers of non-overlapping oriented boxes on the 2080ti (TensorRT FP16).

III. ANALYSIS OF ROTATED NMS FOR DETECTORS

Rotated Non-Maximum Suppression (NMS) is a post-processing algorithm designed to remove overlapping oriented boxes in non-end-to-end oriented object detectors. Rotated NMS requires two thresholds: a rotated IoU threshold and a confidence threshold. It first filters out predicted oriented boxes whose scores fall below the confidence threshold. Then, whenever the rotated IoU between two oriented boxes exceeds the rotated IoU threshold, the box with the lower score is discarded. This process continues until all boxes have been processed. The latency of rotated NMS is influenced by the two thresholds and the number of oriented boxes.

To analyze these effects, we count how many oriented boxes remain after filtering the predictions with different confidence thresholds (0.005 to 0.25) on the DOTA-v1.0 *trainval* set. We adopt anchor-free detectors, RTMDet-s [2] and YOLOX-s [37], and the anchor-based YOLOv5-s [38]. The results in Fig. 2 show that rotated NMS is highly sensitive to the confidence threshold. As the confidence threshold increases, more oriented boxes are removed, leaving fewer candidates for the rotated IoU computation. In addition, we evaluate the AP₅₀ of RTMDet-s on the DOTA-v1.0 *test* set under different thresholds, as shown in Table I. The results show that the detection accuracy is influenced by both thresholds.

Furthermore, we test the execution time of the rotated NMS operation under different numbers of non-overlapping oriented boxes, with a single class and all scores set to 100%, as shown in Fig. 3. The test is conducted on an 2080ti GPU using TensorRT FP16 with NVIDIA `trtexec` and Nsight Systems. The rotated NMS operation adopted here is the `RotatedNMSPlugin` , which is provided as a TensorRT static plugin. Its key kernels include `RotatedNMS`, `RotatedNMSFilter`, and `RadixSort`. As the number of oriented boxes increases, the execution time of `RotatedNMS` grows significantly, whereas the overhead of the other two kernels remains negligible.

IV. METHOD

A. Overview

Our approach is centered on addressing the challenges caused by rotation transformations, including angle representation (Sec. IV-B), matching cost (Sec. IV-C), and training

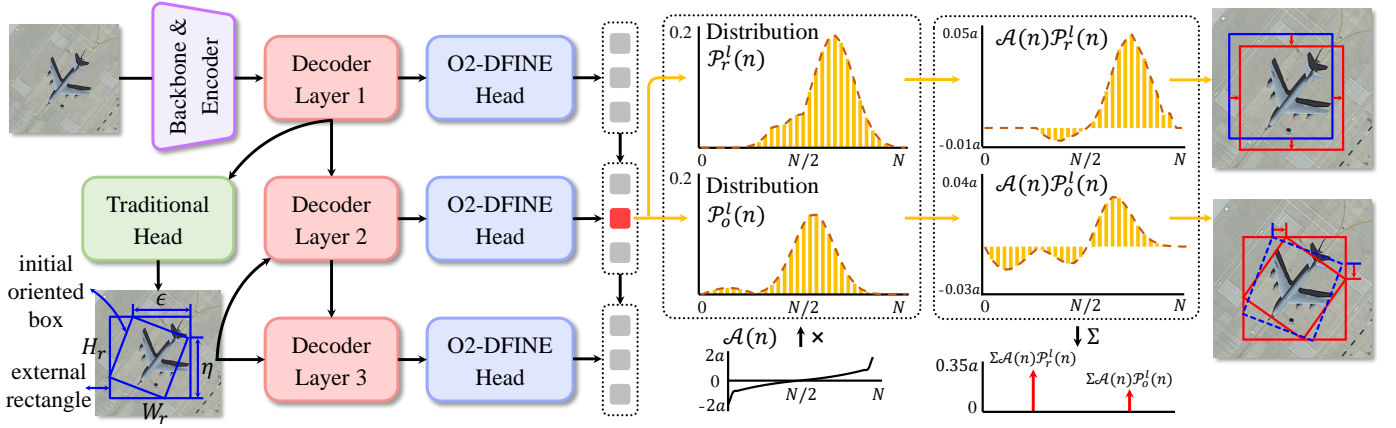


Fig. 4. Overview of O²-DFINE with Angle Distribution Refinement. Oriented boxes are learned in a decoupled manner using probability distributions as fine-grained representations of the external rectangle and vertex offsets, which are iteratively refined across decoder layers in a residual fashion.

stability (Sec. IV-D). The training procedure is shown in Algorithm 1. The model architecture is introduced below.

Oriented boxes definition. We represent an oriented bounding box as (c_x, c_y, w, h, θ) , where (c_x, c_y) denotes the box center, w and h are the width and height, and $\theta \in [0, \pi)$ represents the rotation angle relative to the x-axis.

Backbone with channel mapper. The O²-RTDETR and O²-DEIM adopts the ResNet [39] series as the backbone, while O²-DFINE employs the HGNetv2 [40] series. Both backbones output three feature maps with downsampling ratios of $8\times$, $16\times$, and $32\times$ relative to the input image. To ensure consistent feature dimensions for the encoder, each feature map is projected to 256 channels using a 1×1 convolution layer.

Transformer encoder with query selection. The encoder follows the hybrid encoder [11], decoupling intra-scale interaction and cross-scale fusion. An attention-based module performs self-attention on the highest-level feature map, while a CNN-based module fuses features across scales efficiently. The uncertainty-minimal query selection [11] is employed to select the top- K (default 300) queries, and the corresponding oriented boxes are used as references for the decoder.

Transformer decoder. The decoder consists of multiple stacked decoder layers, each containing self-attention, cross-attention, and feed-forward networks. In cross-attention, the sampling points are rotated around the box center according to the predicted box angle.

Algorithm 1 Training procedure pseudocode.

```
# adr - head with angle distribution refinement
# ocd - oriented contrastive denoising
# cdc - matching with Chamfer distance cost
prediction = adr(transformer(backbone(image)))
noise = ocd(gt) # gt - ground truth
pairs = cdc({prediction, gt}, {noise, gt})
loss(pairs)
```

B. Angle Distribution Refinement

Angle Distribution Refinement (ADR) iteratively optimizes the fine-grained distributions of the rotation angle θ and the parameters (c_x, c_y, w, h) across decoder layers, as shown in Fig. 4. Instead of directly modeling the angle θ in the

angular space, ADR decomposes the prediction process into two stages: (1) refining the external rectangle of an oriented box, and (2) adjusting the vertex offsets along its edges to derive the final oriented box. This indirect formulation ensures that both the angle θ and the parameters (c_x, c_y, w, h) are optimized within a unified metric space, thus avoiding inconsistency. The first decoder layer predicts initial oriented boxes through a traditional oriented box regression head and initial distributions through an O²-DFINE head. Each oriented box is associated with six distributions: four for the edges of its external rectangle and two for the offsets along these edges. The subsequent layers iteratively refine both types of distributions in a residual manner. The refined distributions are used to adjust the external rectangle and its edge offsets, jointly refining the angle θ and the parameters (c_x, c_y, w, h) .

Vertex offset. The initial vertex offsets $\mathcal{D}_o^0 = (\epsilon, \eta)$ are defined such that ϵ measures the distance from the top vertex of the oriented box to the top-right corner of its external rectangle, while η measures the distance from the rightmost vertex to the bottom-right corner. The vertex offsets (ϵ, η) characterize how the oriented box is positioned within its external rectangle. For the l -th decoder layer, the vertex offsets $\mathcal{D}_o^l = (\epsilon^l, \eta^l)$ are updated in a residual manner as:

$$\mathcal{D}_o^l = \mathcal{D}_o^0 + (W_r, H_r) \cdot \sum_{n=0}^N \mathcal{A}(n) \mathcal{P}_o^l(n), \quad (1)$$

where the decoder layer $l \in \{1, 2, \dots, L\}$. $\mathcal{P}_o^l(n) = \{\mathcal{P}_\epsilon^l(n), \mathcal{P}_\eta^l(n)\}$ denotes two distributions corresponding to vertex offset. Each distribution predicts the likelihood of candidate offset values. These candidate offsets are discretized into $N + 1$ bins indexed by n , with each bin representing one possible offset value. The weighting function $\mathcal{A}(n)$ maps each bin index n to its corresponding offset.

External rectangle. Let $r^0 = (c_x, c_y, W_r, H_r)$ denote the initial external rectangle converted from the initial oriented boxes, where (c_x, c_y) is the center and (W_r, H_r) represent the width and height of the external rectangle. Let $\mathcal{D}_r^0 = (\alpha, \beta, \gamma, \delta)$ denote the distances from the center to the left, top, right, and bottom edges of the external rectangle, respec-

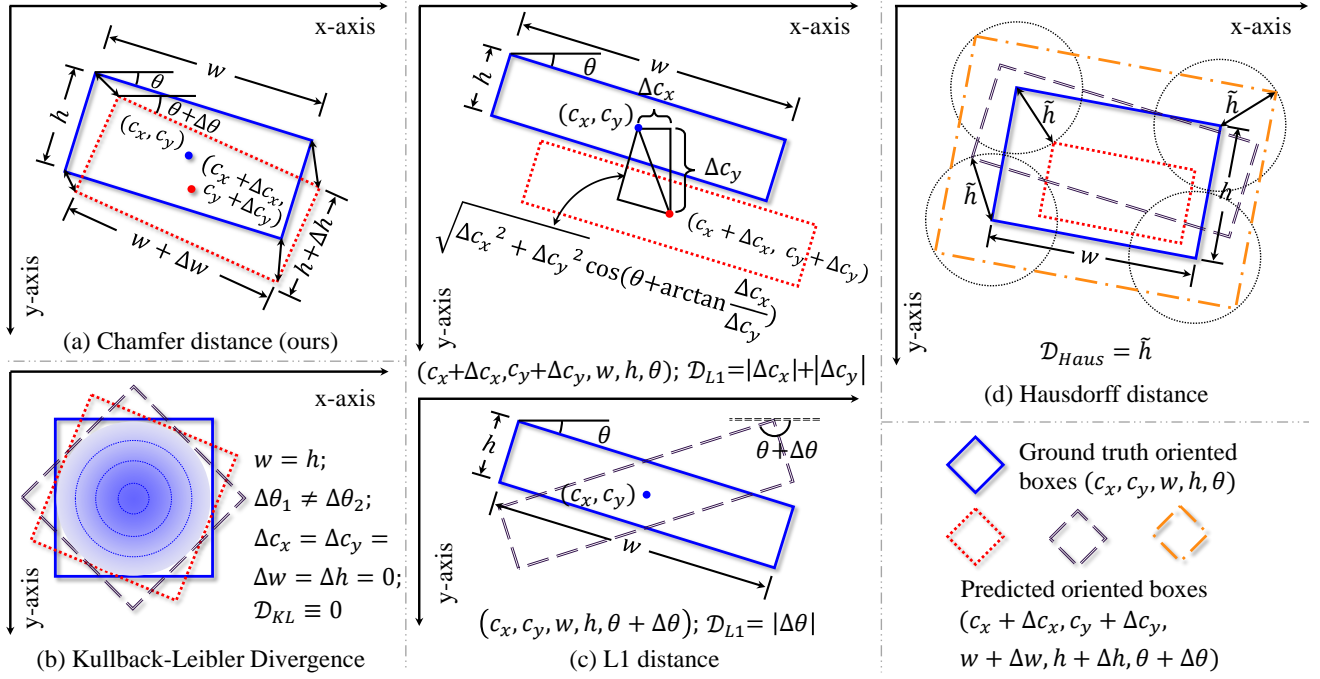


Fig. 5. Distance cost for bipartite matching. (a) Chamfer distance (ours). (b) Kullback-Leibler Divergence. (c) L1 distance. (d) Hausdorff distance.

tively. For the l -th decoder layer, the refined edge distances $\mathcal{D}_r^l = (\alpha^l, \beta^l, \gamma^l, \delta^l)$ are updated in a residual manner as:

$$\mathcal{D}_r^l = \mathcal{D}_r^0 + (W_r, H_r, W_r, H_r) \cdot \sum_{n=0}^N \mathcal{A}(n) \mathcal{P}_r^l(n), \quad (2)$$

where $\mathcal{P}_r^l(n) = \{\mathcal{P}_\alpha^l(n), \mathcal{P}_\beta^l(n), \mathcal{P}_\gamma^l(n), \mathcal{P}_\delta^l(n)\}$ denotes four distributions corresponding to the edges of the external rectangle.

Refined probability distribution. ADR refines the probability distributions in a residual manner, formulated as:

$$\mathcal{P}^l(n) = \text{Softmax}(\text{logits}^{l-1}(n) + \Delta \text{logits}^l(n)). \quad (3)$$

The $\text{logits}^{l-1}(n)$ represent the confidence of the previous decoder layer in each discretized bin of the distance values for the vertex offsets and external rectangle. The current decoder layer outputs residual $\Delta \text{logits}^l(n)$, and the updated logits are computed as $\text{logits}^l(n) = \text{logits}^{l-1}(n) + \Delta \text{logits}^l(n)$. These updated logits are then transformed into refined probability distributions via softmax normalization.

Weighting function. The weighting function is defined as:

$$\mathcal{A}(n) = \text{sgn}(n - \frac{N}{2}) \cdot \begin{cases} 2a, & n \in \{0, N\}, \\ c \left(\left(1 + \frac{a}{c} \right)^{\frac{2|n - \frac{N}{2}|}{N-2}} - 1 \right), & \text{other.} \end{cases} \quad (4)$$

where $n \in \{0, 1, \dots, N\}$ and $\text{sgn}(\cdot)$ denotes the sign function. a and c are hyper-parameters that control the curvature and bounds of the weighting function. When the predicted box is close to the target, the smooth variation of $\mathcal{A}(n)$ enables fine-grained adjustments. In contrast, for inaccurate predictions, the sharp changes near the boundaries of $\mathcal{A}(n)$ allow larger corrective updates.

Loss. The Fine-Grained Localization loss [14] is adopted and applied to both vertex offsets and external rectangle.

C. Chamfer distance cost for bipartite matching

In detection transformers, label assignment is formulated as a bipartite matching problem solved by the Hungarian algorithm. The matching cost typically consists of three terms: distance, IoU, and classification costs. The distance cost measures the spatial alignment between predictions and ground truths. This section focuses on the distance cost, analyzing the limitations of commonly used formulations and introducing the Chamfer distance cost as a more robust and geometry-consistent alternative, as shown in Fig. 5.

Chamfer distance. Chamfer distance is a metric used to measure the similarity between two point sets by calculating the sum of the squared distances from each point in one cloud to its nearest neighbor in the other cloud. Given two point sets \mathcal{S} and \mathcal{T} , it is defined as:

$$\mathcal{D}_{\text{cf}}(\mathcal{S}, \mathcal{T}) = \frac{1}{|\mathcal{S}|} \sum_{s \in \mathcal{S}} \min_{t \in \mathcal{T}} \|s - t\|_2^2 + \frac{1}{|\mathcal{T}|} \sum_{t \in \mathcal{T}} \min_{s \in \mathcal{S}} \|t - s\|_2^2. \quad (5)$$

The first term measures the distance from each point in set \mathcal{S} to its nearest neighbor in \mathcal{T} , while the second term performs the reverse, ensuring symmetry by measuring distances from \mathcal{T} to \mathcal{S} .

Chamfer distance cost. Both the predicted and ground-truth oriented boxes are converted into point sets composed of their four corner vertices, denoted as $\mathcal{S}_{\text{pred}}$ and \mathcal{S}_{gt} . Given an oriented box parameterized by (c_x, c_y, w, h, θ) , its four vertices $\{v_1, v_2, v_3, v_4\}$ can be derived as:

$$v_i = (c_x, c_y) \pm \frac{w}{2} (\cos \theta, \sin \theta) \pm \frac{h}{2} (-\sin \theta, \cos \theta), \quad (6)$$

where $i \in \{1, 2, 3, 4\}$. The ordering of vertices is not constrained, as the Chamfer distance is permutation-invariant with

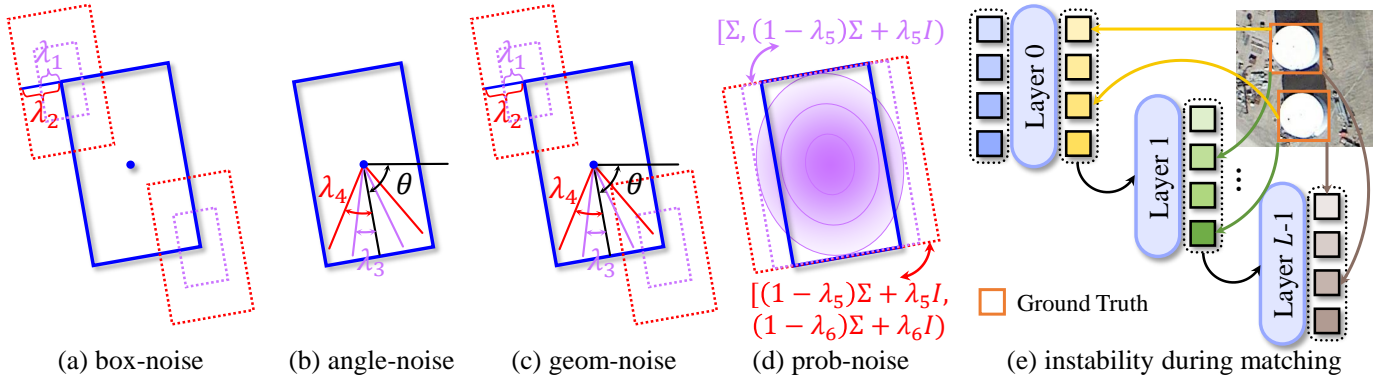


Fig. 6. Oriented Contrastive Denoising. (a) Box noise. (b) Angle noise. (c) Geometric noise. (d) Probability noise. (e) Instability during matching.

respect to point correspondence. The Chamfer distance cost between the two sets is computed as:

$$C_{cf} = D_{cf}(\mathcal{S}_{pred}, \mathcal{S}_{gt}). \quad (7)$$

During bipartite matching, this Chamfer distance cost serves as the distance term in the overall matching cost. The point-based Chamfer distance cost preserves geometric alignment and mitigates matching ambiguity. The following discusses the limitations of conventional cost formulations and the advantages of our proposed method.

Geometric Ambiguity in L1 distance cost. The L1 distance measures absolute differences in center coordinates, widths, heights, and angles. Given a ground-truth box (c_x, c_y, w, h, θ) and a predicted one $(c_x + \Delta c_x, c_y + \Delta c_y, w + \Delta w, h + \Delta h, \theta + \Delta \theta)$, the L1 distance between them is defined as:

$$D_{L1} = |\Delta c_x| + |\Delta c_y| + |\Delta w| + |\Delta h| + |\Delta \theta|. \quad (8)$$

Fig. 5(c) illustrates the geometric ambiguity of the L1 distance. A predicted box $(c_x + \Delta c_x, c_y + \Delta c_y, w, h, \theta)$ that is far away from the ground truth and has zero IoU can still obtain a smaller L1 cost than another prediction $(c_x, c_y, w, h, \theta + \Delta \theta)$ that is perfectly aligned in position and size but differs only by a rotation. The geometric relationships are expressed as:

$$\sqrt{\Delta c_x^2 + \Delta c_y^2} \cos(\theta + \arctan \frac{\Delta c_x}{\Delta c_y}) > h, \quad (9)$$

$$|\Delta \theta| > |\Delta c_x| + |\Delta c_y|. \quad (10)$$

When both Eq. 9 and Eq. 10 are satisfied, the distant prediction $(c_x + \Delta c_x, c_y + \Delta c_y, w, h, \theta)$ obtains a lower L1 cost than the prediction that is rotated by $\Delta \theta$. In contrast, our Chamfer distance assigns a higher cost to the distant prediction and avoids this geometric ambiguity.

Square problem in KL divergence cost. The Kullback-Leibler divergence treats oriented boxes as probability distributions and measures the distance between them [16], as shown in Fig. 5(b). For a square box (c_x, c_y, w, w, θ) , the means of its distribution is $\mu = (c_x, c_y)^\top$ and the variance matrix is $\Sigma = \begin{pmatrix} w^2/4 & 0 \\ 0 & w^2/4 \end{pmatrix}$. Two square boxes that differ only in angle have the same mean μ and variance Σ , and the KL divergence between them is computed as follows:

$$D_{KL} = \frac{1}{2}(\mu - \mu)^\top \Sigma^{-1}(\mu - \mu) + \frac{1}{2} \text{tr}(\Sigma^{-1} \Sigma) + \frac{1}{2} \ln \frac{|\Sigma|}{|\Sigma|} - 1. \quad (11)$$

When two rotated square boxes differ only in their angles, their KL divergence becomes 0, making it unable to distinguish between them. In contrast, the Chamfer distance can still provide a meaningful measure of their difference.

Outlier sensitivity in Hausdorff distance cost. The Hausdorff distance measures how far two point sets are from each other by focusing on their worst-case deviation [10]. Given two point sets \mathcal{S} and \mathcal{T} , the Hausdorff distance is defined as the maximum distance from a point in one set to its nearest neighbor in the other set:

$$D_{\text{Haus}} = \max \left\{ \max_{s \in \mathcal{S}} \min_{t \in \mathcal{T}} \|s - t\|_2, \max_{t \in \mathcal{T}} \min_{s \in \mathcal{S}} \|t - s\|_2 \right\}. \quad (12)$$

The first term measures the greatest among all the smallest distances from points in \mathcal{S} to points in \mathcal{T} , while the second term measures the reverse. By taking the maximum of these two, the Hausdorff distance captures the largest mismatch between the two sets. Fig. 5(d) illustrates a case where the Hausdorff distances \hat{h} ($\hat{h} < \frac{h}{2}$) between the predicted and ground-truth boxes are all the same. In contrast, the Chamfer distance is less sensitive to outliers.

D. Oriented Contrastive Denoising

The Oriented Contrastive Denoising (OCD) is specifically designed for oriented boxes as shown in Fig. 6. OCD generates paired positive and negative queries with noise for each ground-truth oriented box, where the positive queries receive slight noise, and the negative ones receive larger noise. Through this denoising process, the decoder learns to recover accurate box geometry and stabilize training. We explore four noise modes across different dimensions of the oriented boxes. The instability metric is proposed to verify effectiveness.

Box noise. In this setting, the angle θ is kept unchanged. Instead of noise addition into (c_x, c_y, w, h) directly, we first convert the oriented box into (x_1, y_1, x_2, y_2) , where $x_1, x_2 = c_x \pm w/2$, and $y_1, y_2 = c_y \pm h/2$. Noise is then added to each coordinate of the vertices, yielding $(x_1 + \Delta x_1, y_1 + \Delta y_1)$ and $(x_2 + \Delta x_2, y_2 + \Delta y_2)$. The noise magnitude is controlled by two hyperparameters λ_1 and λ_2 ($\lambda_1 < \lambda_2$). For the positive query, we apply small noise to each vertex. For the vertex (x_1, y_1) , the noise ranges are defined as:

$$\Delta x_1^{\text{pos}} \in \left[-\frac{\lambda_1 w}{2}, \frac{\lambda_1 w}{2}\right), \quad \Delta y_1^{\text{pos}} \in \left[-\frac{\lambda_1 h}{2}, \frac{\lambda_1 h}{2}\right), \quad (13)$$

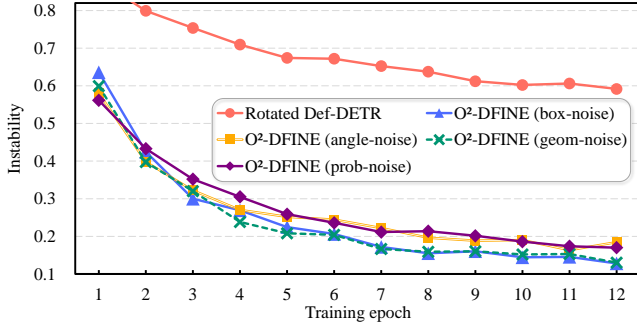


Fig. 7. The instability metric of Oriented Contrastive Denoising.

and the same formulation is applied symmetrically to (x_2, y_2) . This produces a slightly noised oriented box whose shape and location remain close to the ground truth. In contrast, the negative query receives larger noise:

$$\Delta x_1^{\text{neg}} \in \left[-\frac{\lambda_2 w}{2}, -\frac{\lambda_1 w}{2}\right] \cup \left[\frac{\lambda_1 w}{2}, \frac{\lambda_2 w}{2}\right], \quad (14)$$

and similarly for $\Delta y_1^{\text{neg}}, \Delta x_2^{\text{neg}}, \Delta y_2^{\text{neg}}$. These larger vertex shifts produce a significantly distorted box that differs noticeably from the ground truth.

Angle noise. In this setting, noise is only injected into the angle θ while the parameters (c_x, c_y, w, h) remain unchanged. For each ground-truth oriented box, we generate paired positive and negative queries by injecting angular noise, controlled by two hyperparameters λ_3 and λ_4 ($\lambda_3 < \lambda_4$). Specifically, the positive query receives a small random noise:

$$\Delta \theta^{\text{pos}} \in \left[-\frac{\lambda_3 \theta}{18}, \frac{\lambda_3 \theta}{18}\right], \quad (15)$$

which produces an oriented box whose orientation remains close to the ground truth. In contrast, the negative query is noised with a larger angular deviation:

$$\Delta \theta^{\text{neg}} \in \left[-\frac{\lambda_4 \theta}{18}, \frac{\lambda_3 \theta}{18}\right] \cup \left[\frac{\lambda_3 \theta}{18}, \frac{\lambda_4 \theta}{18}\right], \quad (16)$$

resulting in a clearly misaligned orientation.

Geometric noise. The geometric noise setting combines the box noise and angle noise, jointly applying noise to both the box geometry and the rotation angle. Specifically, the parameters (c_x, c_y, w, h) are first converted into (x_1, y_1, x_2, y_2) , and geometric noise is added to the vertices following the box noise strategy. At the same time, the angle θ is perturbed following the angle noise formulation.

Probability noise. Inspired by ReDiffDet [22], each oriented box is represented as a Gaussian distribution $\mathcal{N}(\mathbf{0}, \Sigma)$, where the box center is placed at the origin, and the covariance is defined as $\Sigma = \mathbf{R}\mathbf{A}\mathbf{R}^T$, where $\mathbf{R} = \begin{pmatrix} \cos \theta & -\sin \theta \\ \sin \theta & \cos \theta \end{pmatrix}$ and $\mathbf{A} = \text{diag}\left(\left(\frac{w}{\max(w, h)}\right)^2/4, \left(\frac{h}{\max(w, h)}\right)^2/4\right)$. A standard Gaussian noise $\mathcal{N}(\mathbf{0}, \mathbf{I})$ is added to the distribution. Using the additive property of Gaussian variables, we obtain:

$$\sqrt{1-\lambda}\mathcal{N}(\mathbf{0}, \Sigma) + \sqrt{\lambda}\mathcal{N}(\mathbf{0}, \mathbf{I}) = \mathcal{N}(\mathbf{0}, (1-\lambda)\Sigma + \lambda\mathbf{I}). \quad (17)$$

Two coefficients λ_5 and λ_6 ($\lambda_5 < \lambda_6$) control the perturbation strength for positive and negative queries. The covariance of a positive query is sampled from $\Sigma^{\text{pos}} \in [\Sigma, (1-\lambda_5)\Sigma + \lambda_5\mathbf{I}]$,

TABLE II
MAIN HYPERPARAMETER OF OUR DETECTORS.

Setting	O ² -RTDETR			O ² -DFINE		
	R18	R34	R50	S	M	L
Optimizer	AdamW	AdamW	AdamW	AdamW	AdamW	AdamW
Base LR	1e-4	1e-4	1e-4	5e-5	5e-5	6.25e-5
Backbone LR	1e-5	1e-5	1e-5	2.5e-6	5e-6	3.125e-5
Weight decay	1e-4	1e-4	1e-4	1e-4	1e-4	1.25e-4
Clip grad	0.1	0.1	0.1	0.1	0.1	0.1
Queries K	300	300	300	300	300	300
Layers L	6	6	6	3	4	6
Batchsize	8	8	8	8	8	8
Epochs	72	72	72	72	72	72

while negative queries use $\Sigma^{\text{neg}} \in [(1-\lambda_5)\Sigma + \lambda_5\mathbf{I}, (1-\lambda_6)\Sigma + \lambda_6\mathbf{I}]$. Finally, the noised oriented box is reconstructed from the perturbed covariance via eigenvalue decomposition.

Effectiveness. Fig. 6(e) shows that a single ground-truth object can be matched to different index queries across decoder layers. For a training image, we denote M ground truth objects as $\{\text{gt}_0, \text{gt}_1, \dots, \text{gt}_{M-1}\}$, and predicted objects from l -th decoder layer as $\{\text{query}_0^l, \text{query}_1^l, \dots, \text{query}_{K-1}^l\}$. After bipartite matching, we compute an index vector $\mathbf{G}^l = \{G_0^l, G_1^l, \dots, G_{M-1}^l\}$ to store the matching result of l -th layer as follows:

$$G_m^l = k, \quad \text{if } \text{gt}_m \text{ matches } \text{query}_k^l. \quad (18)$$

We define the instability for one training image as the difference among $\{\mathbf{G}^0, \mathbf{G}^1, \dots, \mathbf{G}^{L-1}\}$, which is calculated as:

$$IS = \left(\sum_{m=0}^{M-1} G_m^0 \oplus G_m^1 \cdots \oplus G_m^{L-1}\right)/M, \quad (19)$$

where \oplus is Exclusive OR. If the matching query indices change across layers, IS will count them. Fig. 7 shows a comparison of instability between rotated Deformable DETR and O²-DFINE-L with different noise modes. We conduct this evaluation on the DOTA-v1.0 trainval set during training 1-12 epochs. The Oriented Contrastive Denoising effectively alleviates the instability of matching.

V. EXPERIMENTS

A. Datasets

We conduct extensive experiments on four datasets DOTA-v1.0 [41], DOTA-v1.5, DIOR-R [42], FAIR1M-v1.0 [43]. DOTA-v1.0 [41] contains 1,869 images in the trainval set and 937 images in the test set, with 188,282 instances annotated across 15 common object categories. DOTA-v1.5 uses the same images and splits as DOTA-v1.0 but includes more small objects and a new class, resulting in 16 categories and 403,318 instances. The DIOR-R [42] dataset comprises 11,725 images in the trainval set and 11,738 in the test set, covering 20 object categories and 192,512 annotated instances. The FAIR1M-v1.0 [43] dataset contains 15,266 high-resolution remote sensing images, encompasses 37 fine-grained object categories organized under 5 coarse categories, and provides over 1.02 million annotated instances.

TABLE III

PERFORMANCE COMPARISONS ON THE **DOTA-v1.0** DATASET. * INDICATES MULTI-SCALE TRAINING AND TESTING. FLOPS ARE COMPUTED FOR AN INPUT SIZE OF (1,3,1024,1024). FPS IS MEASURED ON AN NVIDIA RTX 2080Ti USING TENSORRT IN FP16 MODE WITH AN INPUT SIZE OF (1,3,1024,1024). THE **BEST** AND SECOND-BEST RESULTS ARE HIGHLIGHTED IN **BOLD** AND UNDERLINED.

Methods	Back.	#P	FLOPs	FPS	Pre.	PL	BD	BR	GTF	SV	LV	SH	TC	BC	ST	SBF	RA	HA	SP	HC	AP ₅₀
▼ Non-real-time Oriented Object Detectors																					
ARS-DETR [8]	R50	41M	407G	-	IN	86.97	75.56	48.32	69.20	77.92	77.94	87.69	90.50	77.31	82.86	60.28	64.58	74.88	71.76	66.62	74.16
RO ² -DETR [28]	R50	-	-	-	IN	88.98	82.13	54.58	76.28	79.28	77.92	87.94	90.90	87.19	85.65	62.20	62.63	74.62	72.42	59.22	77.57
O-DETR [7]	R50	57M	563G	-	coco	89.20	86.40	<u>57.70</u>	75.30	81.10	84.70	<u>89.10</u>	90.90	86.10	87.00	59.50	70.30	79.30	81.50	68.80	79.10
MessDet [19]	CSPnext	13M	191G	-	IN	89.28	84.69	<u>56.20</u>	66.18	81.37	85.33	88.86	90.78	88.28	87.62	64.47	65.59	78.18	82.10	67.82	78.45
ReDiffDet [22]	ReR50	-	-	-	IN	86.32	78.72	51.56	71.89	80.05	84.73	88.75	90.84	85.92	86.69	59.48	57.74	75.19	68.43	65.37	75.45
FRED [44]	ReR50	-	-	-	IN	89.37	82.12	50.84	73.89	77.58	77.38	87.51	90.82	86.30	84.25	62.54	65.10	72.65	69.55	63.41	75.56
GauCho* [45]	R50	55M	505G	-	IN	88.96	81.01	57.39	72.21	82.40	85.41	88.51	90.85	85.42	86.40	66.42	70.19	76.10	80.42	71.00	78.85
ACM* [46]	R50	-	-	-	IN	<u>89.84</u>	85.50	53.84	74.78	80.77	82.81	88.92	90.82	87.18	86.53	64.09	66.27	77.51	79.62	69.57	78.53
GSDet [21]	R50	106M	433G	-	IN	88.57	81.17	51.70	73.19	80.22	83.54	88.61	90.82	84.10	81.59	59.48	64.69	75.08	70.00	63.33	75.74
O-RCNN [1]	R50	41M	450G	-	IN	89.46	82.12	54.78	70.86	78.93	83.00	88.20	90.90	87.50	84.68	63.97	67.69	74.94	68.84	52.28	75.87
O-RCNN [1]	PKI [47]	31M	407G	-	IN	89.72	84.20	55.81	77.63	80.25	84.45	88.12	90.88	87.57	86.07	66.86	70.23	77.47	73.62	62.94	78.39
O-RCNN [1]	LSK [48]	31M	375G	-	IN	89.66	85.52	57.72	75.70	74.95	78.69	88.24	90.88	86.79	86.38	66.92	63.77	77.77	74.47	64.82	77.49
▼ Non-end-to-end Real-time Oriented Object Detectors																					
YOLOX-s [37]	CSP-s	9M	68G	237	none	86.43	82.94	47.92	65.51	78.02	84.97	89.07	90.84	87.99	86.01	58.29	63.63	73.23	69.81	59.51	74.94
YOLOX-m [37]	CSP-m	25M	188G	154	none	86.84	<u>86.40</u>	54.27	70.04	81.03	<u>85.68</u>	89.27	90.71	86.32	86.17	60.31	65.52	75.66	72.68	59.53	76.70
PPYOLOE-s [3]	CRN-s	8M	45G	70	IN	88.80	<u>79.24</u>	45.92	66.88	80.41	<u>82.95</u>	88.20	90.61	82.91	86.37	55.80	64.11	65.09	79.50	50.43	73.82
PPYOLOE-m [3]	CRN-m	23M	131G	55	IN	89.23	79.92	51.14	72.94	81.86	84.56	88.68	90.85	86.85	87.48	59.16	68.34	73.78	81.72	68.10	77.64
PPYOLOE-l [3]	CRN-l	52M	291G	48	IN	89.18	81.00	54.01	70.22	81.85	85.16	88.81	90.81	86.99	88.01	62.87	67.87	76.56	79.13	69.65	78.14
YOLOv5-n [38]	CSP-n	2M	13G	108	coco	89.82	75.73	44.75	62.78	79.91	82.80	87.91	90.83	79.15	87.12	50.54	63.11	67.49	80.07	56.87	73.26
YOLOv5-s [38]	CSP-s	8M	45G	98	coco	89.26	84.53	51.36	60.69	80.70	84.74	88.41	90.68	85.93	87.59	59.62	65.18	74.53	81.71	66.91	76.79
YOLOv5-m [38]	CSP-m	22M	129G	72	coco	89.60	86.39	54.62	62.04	80.36	85.20	88.40	90.80	80.54	<u>88.47</u>	64.16	61.21	76.70	83.13	67.91	77.30
PSC-s [49]	CSP-s	8M	45G	98	coco	89.65	86.37	51.76	63.42	81.21	84.63	88.29	90.80	85.39	87.93	61.00	66.41	75.01	81.77	66.20	77.32
PSC-m [49]	CSP-m	22M	129G	72	coco	89.85	85.93	54.94	61.56	<u>81.89</u>	85.47	88.37	90.73	86.90	88.79	63.90	68.92	76.82	<u>82.83</u>	63.25	78.01
RTMDet-s [2]	CSP-s	9M	126G	197	IN	89.18	80.45	52.09	71.35	<u>81.55</u>	84.05	88.79	90.89	87.83	86.98	59.58	62.28	75.90	81.96	61.04	76.93
RTMDet-m [2]	CSP-m	25M	314G	120	IN	89.17	84.65	53.92	74.67	81.48	83.99	88.71	90.85	87.43	87.20	59.39	66.68	77.71	82.40	65.28	78.24
RTMDet-l [2]	CSP-l	52M	612G	86	IN	89.43	84.21	55.20	75.06	80.81	84.53	88.97	90.90	87.38	87.25	63.09	67.87	78.09	80.78	69.13	78.85
YOLOMS-xs [4]	MS-xs	4M	73G	139	coco	89.44	84.21	52.63	74.07	81.76	82.51	88.71	90.90	87.66	86.50	63.04	58.84	76.51	69.19	52.18	75.88
YOLOMS-s [4]	MS-s	8M	131G	100	coco	89.37	83.92	53.26	73.54	81.75	84.94	88.91	90.89	<u>88.34</u>	87.86	61.99	56.97	77.54	75.65	53.26	76.55
▼ End-to-end Real-time Oriented Object Detection																					
RTDETR-R	R18	20M	147G	233	IN	86.20	69.96	50.33	70.66	78.79	84.32	87.40	90.28	85.05	77.55	52.01	56.58	76.27	79.82	63.89	73.94
RTDETR-R	R34	31M	228G	174	IN	87.24	78.31	51.37	70.85	79.54	83.75	87.31	90.02	86.71	84.64	57.25	61.18	76.22	70.09	58.69	74.88
RTDETR-R	R50	42M	339G	119	IN	87.46	77.98	51.60	72.06	79.66	84.10	87.72	90.29	87.32	84.81	57.37	60.28	76.59	71.37	60.29	75.26
O ² -RTDETR	R18	20M	147G	233	IN	88.96	84.23	51.98	71.53	80.19	84.98	88.40	90.87	87.86	85.47	57.69	66.27	77.19	74.62	69.42	77.31
O ² -RTDETR	R34	31M	228G	174	IN	88.88	83.77	53.75	73.90	80.76	85.36	88.61	90.87	86.64	86.75	58.31	66.44	77.25	80.07	70.68	78.13
O ² -RTDETR	R50	42M	339G	119	IN	89.27	84.06	56.50	75.85	80.02	84.06	88.05	90.85	85.32	86.68	63.19	64.96	77.76	77.80	72.38	78.45
O ² -DEIM*	R18	20M	147G	233	coco	88.60	83.38	54.00	79.62	80.13	85.93	88.57	90.90	88.11	85.77	67.55	66.67	77.11	77.99	77.96	79.49
O ² -DEIM*	R34	31M	228G	174	coco	88.03	84.62	56.97	<u>80.02</u>	81.05	84.74	88.62	<u>90.90</u>	88.54	86.86	<u>68.80</u>	<u>68.86</u>	80.28	79.00	73.27	<u>80.04</u>
O ² -DEIM*	R50	42M	339G	119	coco	88.14	84.89	57.13	80.34	81.21	84.54	88.67	90.90	88.31	86.97	69.83	68.80	<u>80.20</u>	78.71	<u>73.56</u>	80.15
DFINE-R-s	HG-B0	10M	60G	297	IN	85.75	62.29	47.76	67.69	79.62	80.99	87.60	90.30	82.41	78.69	57.09	55.67	74.43	72.62	63.63	72.44
DFINE-R-m	HG-B2	19M	142G	176	IN	86.33	69.91	49.68	66.18	79.69	84.47	88.28	90.85	87.80	78.41	55.04	52.89	76.32	71.66	71.31	73.92
DFINE-R-l	HG-B4	31M	229G	132	IN	85.72	72.69	50.50	66.14	79.76	84.55	88.30	90.90	86.52	77.60	55.50	55.61	75.89	71.95	69.78	74.09
O ² -DFINE-s	HG-B0	10M	60G	297	IN	88.84	75.59	53.97	69.09	80.02	85.02	88.51	90.85	87.71	87.63	56.32	63.23	77.10	69.23	68.88	76.14
O ² -DFINE-m	HG-B2	19M	142G	176	IN	89.42	81.80	53.92	72.89	79.42	83.90	88.21	90.88	86.56	86.42	58.51	66.03	77.41	78.28	70.46	77.61
O ² -DFINE-l	HG-B4	31M	229G	132	IN	89.08	80.18	55.17	69.73	80.53	83.77	88.46	90.86	87.55	86.86	60.14	68.68	77.17	77.79	70.03	77.73

B. Implementation Details and Evaluation Metrics

Implementation details. We conduct all the experiments on two 🍷 2080ti with a batch of 8 (4 images per GPU). Models are constructed based on AI4RS with Pytorch 🔥. We optimize models with the AdamW optimizer. O²-RTDETR and O²-DEIM employ KLD loss \mathcal{L}_{kld} [16], focal loss \mathcal{L}_{focal} [15], and L1 loss \mathcal{L}_{L1} , while O²-DFINE further incorporates an additional Fine-Grained Localization (FGL) loss \mathcal{L}_{fgl} [14]. The weights of losses are $\lambda_{kld} = 2.0$, $\lambda_{cls} = 1.0$, $\lambda_{L1} = 5.0$, and $\lambda_{fgl} = 0.15$ respectively. Overall loss is calculated as $\lambda_{kld}\mathcal{L}_{kld} + \lambda_{cls}\mathcal{L}_{focal} + \lambda_{L1}\mathcal{L}_{L1} + \lambda_{fgl}\mathcal{L}_{fgl}$. The distillation loss is not used. The weights of cost are $\xi_{kld} = 2.0$, $\xi_{cls} = 2.0$, and $\xi_{cf} = 5.0$ for KLD cost \mathcal{C}_{kld} , focal cost \mathcal{C}_{focal} , and Chamfer distance cost \mathcal{C}_{cf} . Overall cost is calculated as $\xi_{kld}\mathcal{C}_{kld} + \xi_{cls}\mathcal{C}_{focal} + \xi_{cf}\mathcal{C}_{cf}$. Details of experiments are displayed in Table II.

For experiments on the DOTA and FAIR1M, images are cropped into 1024×1024 patches with an overlap of 200. For multi-scale training on DOTA-v1.0, each image is first resized to three scales (0.5, 1.0, and 1.5) and then cropped following

single-scale training. For DIOR-R, images are used at the original fixed size of 800×800 . For DOTA and FAIR1M, we submit test predictions to their official evaluation servers to obtain the final performance. DOTA uses both random flips and random rotations for data augmentation, while DIOR-R and FAIR1M apply only random flips.

Evaluation metrics. Average Precision (AP) evaluates detection accuracy by integrating the precision-recall curve over different confidence thresholds. The parameter count measures the number of learnable weights in the model. FLOPs represent the total number of floating-point operations required for a single forward pass. FPS reflects the inference speed by reporting how many images are processed per second. Latency is the time required to process one image, and it is inversely related to FPS.

C. Comparisons with modern oriented object detector

Results on DOTA-v1.0. Table III summarizes the experimental results on the DOTA-v1.0. O²-DFINE-s / m / l achieve AP₅₀ of 76.14%, 77.61%, and 77.73%, respectively, consistently outperforming the corresponding DFINE-R baselines.

TABLE IV

PERFORMANCE COMPARISONS ON THE **DIOR-R** DATASET. THE **BEST** AND **SECOND-BEST** RESULTS ARE HIGHLIGHTED IN **BOLD** AND UNDERLINED.

Method	Back.	#P	APL	APO	BF	BC	BR	CH	DAM	ETS	ESA	GF	GTF	HA	OP	SH	STA	STO	TC	TS	VE	WM	AP ₅₀
RoI Trans. [50]	R50	55M	63.34	37.88	71.78	87.53	40.68	72.60	26.86	<u>78.71</u>	68.09	68.96	82.74	47.71	55.61	81.21	<u>78.23</u>	70.26	81.61	54.86	43.27	65.52	63.87
O-RCNN [1]	R50	41M	71.10	39.30	79.50	86.20	43.10	72.60	29.50	66.70	79.30	68.60	82.40	43.60	57.60	81.30	74.20	62.60	81.40	54.80	46.80	66.00	64.30
AOPG [42]	R50	-	62.39	37.79	71.62	87.63	40.90	72.47	31.08	65.42	77.99	73.20	81.94	42.32	54.45	81.17	72.69	71.31	81.49	60.04	52.38	69.99	64.41
ARS-DETR [8]	R50	41M	68.00	54.17	74.43	81.65	41.13	75.66	34.89	73.07	81.92	76.10	78.62	36.33	55.41	84.55	70.09	72.23	81.14	61.52	50.57	70.28	66.12
RO ² -DETR [28]	R50	-	69.78	54.77	74.49	82.11	42.30	76.66	33.94	72.99	82.01	76.11	78.56	40.11	56.06	85.06	73.11	72.19	84.10	60.66	53.02	71.11	66.43
OrientedRep [51]	R50	36M	70.03	46.11	76.12	87.19	39.14	78.76	34.57	71.80	80.42	76.16	79.41	45.48	54.90	87.82	77.03	68.07	81.60	56.83	51.57	71.25	66.71
DCFL [20]	R50	36M	68.60	53.10	76.70	87.10	42.10	78.60	34.50	71.50	80.80	79.70	79.50	47.30	57.40	85.20	64.60	66.40	81.50	58.90	50.90	70.90	66.80
OFormer [30]	R50	44M	65.65	48.69	78.79	87.17	41.90	76.34	34.37	72.14	81.40	75.34	79.83	45.15	56.12	<u>88.66</u>	67.59	72.68	87.32	60.31	56.54	69.56	67.28
RQFormer [9]	R50	41M	67.31	55.23	74.19	82.74	44.49	78.56	39.85	70.27	79.84	75.10	80.38	45.64	58.51	88.91	68.10	75.73	85.52	57.17	53.54	65.05	67.31
ReDiffDet [22]	ReR50	-	71.36	49.22	71.65	<u>87.88</u>	47.12	79.28	33.35	73.37	83.74	70.29	80.38	43.63	57.17	89.52	72.39	79.81	89.03	57.34	57.32	67.23	68.05
GSDet [21]	R50	106M	81.07	<u>58.94</u>	78.06	85.91	<u>48.64</u>	77.55	42.51	73.25	86.18	75.04	78.98	41.29	<u>59.81</u>	87.54	78.43	76.96	87.22	58.06	<u>57.30</u>	68.25	<u>70.05</u>
O²-RTDETR	R34	31M	71.58	50.71	79.10	83.75	48.09	77.85	37.19	74.22	84.34	75.62	<u>83.01</u>	44.28	59.24	85.51	70.21	75.14	84.63	<u>62.03</u>	54.74	<u>72.17</u>	68.67
O²-RTDETR	R50	42M	79.36	59.61	<u>79.33</u>	88.73	50.80	81.42	<u>42.34</u>	79.64	89.53	78.05	83.95	50.01	61.35	88.46	70.20	71.34	88.47	61.80	59.09	73.02	72.26
O²-DFINE-s	HG-B0	10M	66.89	47.97	<u>77.73</u>	83.51	43.64	78.37	32.82	69.65	84.01	77.17	82.04	45.14	56.78	85.91	73.74	71.63	82.82	62.18	52.62	66.22	67.05
O²-DFINE-m	HG-B2	19M	<u>76.83</u>	51.90	78.22	85.52	46.93	<u>80.79</u>	37.72	77.23	<u>89.24</u>	77.60	82.42	<u>49.78</u>	58.00	87.16	67.20	77.27	86.55	61.01	54.65	71.25	69.86

TABLE V

PERFORMANCE COMPARISONS ON THE **DOTA-v1.5** DATASET. THE **BEST** AND **SECOND-BEST** RESULTS ARE HIGHLIGHTED IN **BOLD** AND UNDERLINED. RESULTS ARE REPORTED UNDER SINGLE-SCALE TRAINING AND TESTING.

Method	Back.	#P	PL	BD	BR	GTF	SV	LV	SH	TC	BC	ST	SBF	RA	HA	SP	HC	CC	AP ₅₀
GauCho [45]	R50	55M	76.42	72.78	48.42	59.72	61.65	75.19	84.83	<u>90.88</u>	76.44	73.88	56.75	69.51	62.98	67.79	50.55	13.65	65.09
ReDet [18]	ReR50	32M	79.20	82.81	51.92	71.41	52.38	75.73	80.92	<u>90.83</u>	75.81	68.64	49.29	72.03	73.36	70.55	63.33	11.53	66.86
DCFL [20]	R50	36M	-	-	-	-	56.72	-	80.87	-	-	75.65	-	-	-	-	-	-	67.37
RQFormer [9]	R50	41M	78.44	75.43	48.84	63.62	62.16	78.41	88.94	90.84	75.29	81.83	57.05	66.44	73.95	72.69	51.64	13.37	67.43
GSDet [21]	R50	106M	<u>80.48</u>	72.51	49.11	71.19	57.75	78.96	88.93	90.85	79.44	77.52	55.77	65.56	71.36	70.40	65.41	10.26	67.84
FRED [44]	R50	-	79.60	81.44	52.60	72.57	58.07	74.82	86.12	90.81	82.13	74.84	53.37	72.93	69.51	69.91	54.82	19.27	68.30
O-RCNN [1]	LSK-s [48]	31M	72.05	84.94	<u>55.41</u>	74.93	52.42	77.45	81.17	90.85	79.44	69.00	62.10	<u>73.72</u>	77.59	75.29	55.81	42.19	70.26
O-RCNN [1]	PKI-s [47]	31M	80.31	<u>85.00</u>	55.61	<u>74.38</u>	52.41	76.85	88.38	90.87	79.04	68.78	67.47	72.45	76.24	74.53	64.07	37.13	71.47
RHINO [10]	R50	48M	77.96	83.22	55.30	72.14	65.07	78.95	89.22	90.78	80.90	83.48	61.58	74.17	77.21	71.99	60.16	29.26	71.96
MessDet [19]	CSPnext	13M	80.61	84.99	54.56	65.36	73.60	82.69	89.73	90.83	82.46	82.03	59.35	72.96	<u>77.66</u>	75.14	65.09	21.12	72.38
RTMDet-s [2]	CSPnext-s	9M	80.05	84.36	50.65	72.04	59.54	81.79	89.22	90.90	<u>83.07</u>	76.27	56.82	72.13	<u>76.25</u>	77.04	65.66	32.84	71.79
RTMDet-m [2]	CSPnext-m	25M	80.34	86.00	54.02	72.98	63.21	<u>82.09</u>	<u>89.46</u>	90.87	85.12	76.69	<u>63.12</u>	72.14	77.91	<u>76.04</u>	71.57	32.24	<u>73.36</u>
O²-RTDETR	R34	31M	73.92	84.31	54.07	69.62	<u>65.92</u>	80.48	88.91	90.82	79.37	80.37	55.95	69.60	74.91	73.70	74.38	<u>34.20</u>	71.91
O²-RTDETR	R50	42M	80.43	83.97	53.37	72.14	66.58	80.10	89.40	90.80	78.94	<u>83.45</u>	58.44	70.38	76.73	75.56	<u>75.11</u>	44.77	73.76
O²-DFINE-s	HG-B0	10M	74.73	81.99	53.87	66.56	64.88	77.82	88.39	90.74	77.57	78.65	55.70	68.69	69.33	70.79	71.07	32.83	70.22
O²-DFINE-m	HG-B2	19M	77.64	84.11	54.08	69.34	65.58	80.77	88.64	90.60	79.13	80.64	57.64	69.86	74.56	73.54	76.19	32.10	72.15

Similarly, O²-RTDETR with R18 / R34 / R50 backbones attains AP₅₀ of 77.31%, 78.13%, and 78.45%, respectively, surpassing the RTDETR-R models. Furthermore, under multi-scale training and testing, O²-DEIM-R18 / R34 / R50 achieve AP₅₀ of 79.49%, 80.04%, and 80.15%, respectively. The compared methods use the same image preprocessing as this chapter. These results demonstrate that our method is highly competitive with both modern non-end-to-end real-time and non-real-time oriented object detectors.

Comparison of FPS, Parameters, FLOPs and Accuracy. Table III shows the comparison in terms of FPS, parameters, FLOPs, and accuracy. All FLOPs are computed with a 1024×1024 input, and FPS is measured on an NVIDIA 2080ti using TensorRT FP16 under the same resolution. O²-DFINE-s reaches 297 FPS with only 10M parameters and 60G FLOPs, while the larger O²-DFINE-m/l variants run at 176/132 FPS with 19M/31M parameters and 142G/229G FLOPs. O²-RTDETR with ResNet-18/34/50 backbones achieves 233/174/119 FPS, using 20M/31M/42M parameters and 147G/228G/339G FLOPs, respectively. The O²-DEIM retains the same FPS, parameter count, and FLOPs as its baseline. Importantly, our approach introduces no additional parameters, latency, or FLOPs, as it focuses on representation and optimization. Our approach is competitive with existing real-time detectors in both efficiency and accuracy.

Results on DIOR-R. The DIOR-R results are summarized in Table IV. Our method achieves consistently strong perfor-

mance across all model variants. O²-DFINE-s attains 67.05% AP₅₀, while the larger O²-DFINE-m further improves the score to 69.86% AP₅₀. For the RTDETR family, O²-RTDETR-R34 obtains 68.67% AP₅₀, and the stronger O²-RTDETR-R50 reaches 72.26% AP₅₀, outperforming all existing oriented DETR-based and two-stage detectors listed in the comparison. These results demonstrate that our oriented modeling brings consistent gains across backbones and model scales.

Results on DOTA-v1.5. As shown in Table V, our proposed models achieve competitive performance on the DOTA-v1.5 dataset. Specifically, O²-DFINE-s attains 70.22% AP₅₀, while O²-DFINE-m reaches 72.15% AP₅₀. Furthermore, O²-RTDETR-R34 achieves 71.91% AP₅₀, and O²-RTDETR-R50 attains 73.76% AP₅₀, outperforming several existing approaches with particularly significant gains on small objects such as helicopters and container cranes.

Results on FAIRIM-v1.0. Table VI presents the performance comparison on the FAIRIM-v1.0 dataset under single-scale training and testing settings. Our methods achieve strong results across the board: O²-DFINE-s obtains an AP₅₀ of 39.77%, and its larger variant O²-DFINE-m further improves this to 42.01%. Moreover, O²-RTDETR with a ResNet-34 backbone achieves 40.45% AP₅₀, while the ResNet-50 version reaches 43.14% AP₅₀, outperforming all existing approaches by a clear margin.

TABLE VI
PERFORMANCE COMPARISONS ON THE **FAIR1M-v1.0** DATASET. THE **BEST** AND SECOND-BEST RESULTS ARE HIGHLIGHTED IN **BOLD** AND UNDERLINED. RESULTS ARE REPORTED UNDER SINGLE-SCALE TRAINING AND TESTING.

Method	Back.	#P	B737	B747	B777	B787	C919	A220	A321	A330	A350	ARJ21	PS	MB	FB	TB	ES	LCS	DCS	
RetinaNet [52]	R101	36M	38.46	55.36	24.75	51.81	0.81	40.50	41.06	18.02	19.94	1.70	9.57	22.55	1.33	16.37	19.11	14.26	24.70	
CasRCNN [53]	R101	69M	40.42	52.86	<u>29.07</u>	52.47	0.00	44.37	38.35	26.55	17.54	0.00	12.10	28.84	0.71	15.35	18.53	14.63	25.15	
FasterRCNN [54]	R101	41M	36.43	50.68	22.50	51.86	0.01	47.81	43.83	17.66	19.95	0.13	9.81	28.78	1.77	17.65	16.47	16.19	27.06	
CHODNet [43]	R101	-	40.23	53.39	29.65	54.04	0.02	46.26	43.12	27.61	20.89	0.01	12.34	29.34	1.71	17.77	17.72	16.78	27.51	
RoITrans [50]	R101	55M	39.58	73.56	18.32	<u>56.43</u>	0.00	47.67	49.91	27.64	31.79	0.00	14.31	28.07	1.03	14.32	15.97	18.04	26.02	
O-RCNN [1]	R50	41M	35.17	85.17	14.57	47.68	11.68	46.55	68.18	68.60	70.21	25.32	13.77	60.42	9.10	36.83	11.32	<u>21.86</u>	38.22	
O²-RTDETR	R34	31M	<u>41.03</u>	85.87	17.00	49.27	23.96	49.74	63.83	67.11	70.60	37.85	<u>14.78</u>	62.73	9.73	30.09	13.28	21.69	39.50	
O²-RTDETR	R50	42M	39.42	86.87	20.94	57.01	<u>26.62</u>	47.68	67.39	67.73	78.37	<u>34.06</u>	15.90	<u>11.60</u>	34.06	19.54	25.25	42.40		
O²-DFINE-s	HG-B0	10M	39.54	84.20	18.60	50.56	25.15	<u>50.17</u>	64.30	68.89	71.81	33.49	12.73	60.65	9.21	29.80	11.20	16.64	35.98	
O²-DFINE-m	HG-B2	19M	41.56	<u>86.38</u>	14.81	53.31	28.37	53.27	71.28	69.75	<u>77.43</u>	27.52	11.58	<u>64.18</u>	12.21	38.86	<u>19.44</u>	20.26	<u>40.59</u>	
Method	Back.	#P	WS	SC	Bus	CT	DT	VAN	TRI	TRC	EX	TT	BC	TC	FF	BF	IS	RA	BR	AP ₅₀
RetinaNet [52]	R101	36M	15.37	65.20	22.42	44.17	35.37	52.44	19.17	1.28	17.03	28.98	50.58	81.09	52.50	66.76	60.13	17.41	12.58	30.67
CasRCNN [53]	R101	69M	14.53	68.19	28.25	48.62	40.40	58.00	13.66	0.91	16.45	<u>30.27</u>	38.81	80.29	48.21	67.90	55.67	20.35	12.62	31.18
FasterRCNN [54]	R101	41M	13.16	68.42	28.37	<u>51.24</u>	43.60	57.51	15.03	3.04	<u>17.99</u>	29.36	58.26	82.67	54.50	71.71	59.86	16.92	11.87	32.12
CHODNet [43]	R101	-	13.68	70.12	28.38	49.11	44.02	60.78	14.48	4.96	17.60	30.09	47.91	82.11	54.10	69.97	59.91	19.57	14.38	32.93
RoITrans [50]	R101	55M	12.97	68.80	<u>37.41</u>	53.96	<u>45.68</u>	58.39	<u>16.22</u>	<u>5.13</u>	22.17	46.71	<u>54.84</u>	80.35	56.68	69.07	58.44	18.58	31.81	35.29
O-RCNN [1]	R50	41M	22.67	57.62	24.40	40.84	45.20	54.01	15.46	2.37	13.55	0.24	48.18	78.45	<u>60.79</u>	<u>88.43</u>	57.90	17.57	28.63	38.85
O²-RTDETR	R34	31M	37.26	66.56	27.34	41.78	42.60	63.13	7.67	1.88	16.10	1.16	44.16	80.83	57.66	87.07	52.52	<u>20.59</u>	28.83	40.45
O²-RTDETR	R50	42M	39.51	<u>68.81</u>	41.23	46.21	48.86	66.31	11.14	3.64	16.31	2.47	47.51	80.36	59.08	88.49	55.19	18.30	33.27	43.14
O²-DFINE-s	HG-B0	10M	34.52	63.41	24.38	38.61	41.19	60.55	7.95	4.71	15.27	0.51	44.04	82.08	58.34	87.30	52.43	22.18	31.89	39.77
O²-DFINE-m	HG-B2	19M	<u>39.13</u>	66.37	24.86	41.82	44.08	<u>63.31</u>	8.67	8.61	12.38	0.95	48.74	<u>82.63</u>	63.21	86.98	54.74	18.97	<u>32.24</u>	<u>42.01</u>

TABLE VII
STEP-BY-STEP IMPROVEMENTS FROM THE BASELINE MODEL TO O²-DFINE-S, O²-RTDETR-R18, AND O²-DEIM-R18 ON DOTA-V1.0.

O ² -DFINE-s	AP ₅₀	#P	FPS	FLOPs
DFINE-R-s	72.44	10M	297	60G
+ oriented contrastive denoising	73.72	10M	297	60G
+ angle distribution refinement	75.05	10M	297	60G
+ Chamfer distance cost	76.14	10M	297	60G
O ² -RTDETR-R18	AP ₅₀	#P	FPS	FLOPs
RTDETR-R-R18	73.94	20M	233	147G
+ oriented contrastive denoising	75.72	20M	233	147G
+ Chamfer distance cost	77.31	20M	233	147G
O ² -DEIM-R18	AP ₅₀	#P	FPS	FLOPs
O ² -RTDETR-R18	77.31	20M	233	147G
+ Matchability-Aware Loss and Multi-scale training	79.49	20M	233	147G

TABLE VIII
ABLATION STUDY OF ANGLE DISTRIBUTION REFINEMENT IN O²-DFINE-S ON DOTA-V1.0.

Number of bins N	8	16	32	64	128
AP ₅₀	75.78	75.86	76.14	75.98	75.91
a, c of $\mathcal{A}(\cdot)$ in (4)	$\frac{1}{4}, \frac{1}{4}$	$\frac{1}{2}, 10$	$\frac{1}{2}, \frac{1}{4}$	$\frac{1}{2}, \frac{1}{8}$	$1, \frac{1}{4}$
AP ₅₀	75.27	75.64	76.14	75.98	75.92

D. Ablation Study

Model Improvement Roadmap. Table VII presents a step-by-step ablation study illustrating how each component contributes to the final performance on DOTA-v1.0. For O²-DFINE-R18, AP₅₀ increases from 72.44% to 76.14% as oriented contrastive denoising, angle distribution refinement, and the Chamfer distance cost are introduced. For O²-RTDETR-s, these components similarly raise AP₅₀ from 73.94% to 77.31%. Adding Matchability-Aware Loss [15] and multi-scale training further improves O²-DEIM-s to 79.49%. Following [15], multi-scale training as data augmentation provides more

TABLE IX
ABLATION STUDY OF THE CHAMFER DISTANCE COST FOR BIPARTITE MATCHING IN O²-DFINE-S ON DOTA-V1.0.

Distance Cost	Cost Weight	Distance Loss	Loss Weight	Point Number	AP ₅₀
KL Divergence	2.0	KLD	2.0	None	73.69
L1	5.0	L1	5.0	None	74.28
Hausdorff	5.0	L1	5.0	4	75.05
Chamfer	5.0	L1	5.0	4	76.14
Chamfer	3.0	L1	3.0	4	75.18
Chamfer	4.0	L1	4.0	4	75.40
Chamfer	5.0	L1	5.0	4	76.14
Chamfer	6.0	L1	6.0	4	75.69
Chamfer	5.0	L1	5.0	4	76.14
Chamfer	5.0	L1	5.0	16	75.80
Chamfer	5.0	L1	5.0	32	75.54

positive objects. All improvements come without extra cost, as our method focuses on detection optimization rather than modifying the feature extraction module.

Number of bins N . Table VIII evaluates the effect of the number of angle bins in the Angle Distribution Refinement. Increasing N from 8 to 32 gradually improves performance, with the best result of 76.14% AP₅₀ achieved at $N = 32$. Further increasing the bin count to 64 or 128 does not provide additional gains and even leads to slight fluctuations.

Weighting function parameters a, c . We examine the hyper-parameters a, c in weighting function $\mathcal{A}(\cdot)$ in Table VIII. When c becomes excessively large, the weighting function degenerates toward a uniformly spaced linear form, which leads to suboptimal AP performance. Moreover, too large or small values of a change the bounds of $\mathcal{A}(\cdot)$, thereby degrading localization accuracy.

Different distance cost. Table IX compares different distance costs for bipartite matching. Using only KL divergence provides the weakest supervision, resulting in 73.69% AP₅₀. In the subsequent experiments, KL divergence is kept as the IoU cost while additional distance terms are introduced. L1 distance yields a moderate improvement to 74.28%, and

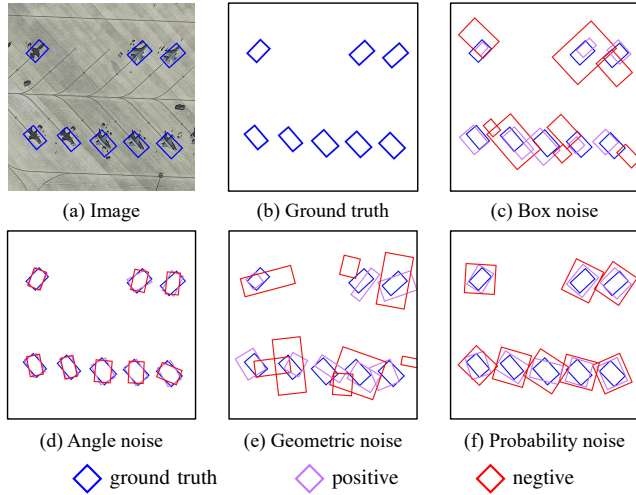


Fig. 8. Qualitative analysis of Oriented Contrastive Denoising. (a) An image example. (b) Ground-truth oriented boxes. (c) The box noise. (d) The angle noise. (e) The geometric noise. (f) The probability noise example.

TABLE X
ABLATION STUDY OF THE ORIENTED CONTRASTIVE DENOISING IN O^2 -DFINE-S ON DOTA-V1.0.

Box noise	λ_1	0.5	1.0	2.0
		λ_2	1.0	2.0
	AP ₅₀	75.33	76.14	75.12
Angle noise	λ_3	3.0	5.0	9.0
	λ_4	6.0	10.0	18.0
	AP ₅₀	74.29	74.53	74.71
Geometric noise	λ_1	0.5	1.0	2.0
	λ_2	1.0	2.0	4.0
	λ_3	9.0	9.0	9.0
	λ_4	18.0	18.0	18.0
	AP ₅₀	75.05	75.72	74.88
Probability noise	λ_5	0.2	0.3	0.4
	λ_6	0.4	0.6	0.8
	AP ₅₀	74.32	74.56	74.49
Box noise	Denoising query	100	200	300
	AP ₅₀	75.83	76.14	76.10

adding geometric information through the Hausdorff distance further boosts accuracy to 75.05%. The Chamfer distance achieves the best performance of 76.14%, showing that it captures oriented object geometry more accurately.

Chamfer distance cost weight. We further examine the effect of the Chamfer distance weight in Table IX. A balanced weight of 5.0 yields the highest 76.14% AP₅₀, whereas smaller weights such as 4.0 and larger weights such as 6.0 lead to slight accuracy degradation. This suggests that unsuitable geometric constraints can disrupt the matching quality.

Point number in Chamfer distance cost. The number of points used in the Chamfer distance is also evaluated in Table IX. Using the four vertices $\{v_1, v_2, v_3, v_4\}$ of the oriented box gives the best performance of 76.14% AP₅₀. When more points are uniformly sampled along the four edges to form 16 or 32 points, the accuracy slightly decreases. This is because the four vertices already represent the convex hull of the box, and adding edge points increases the size of the point sets for both predictions and ground truths, causing small fluctuations

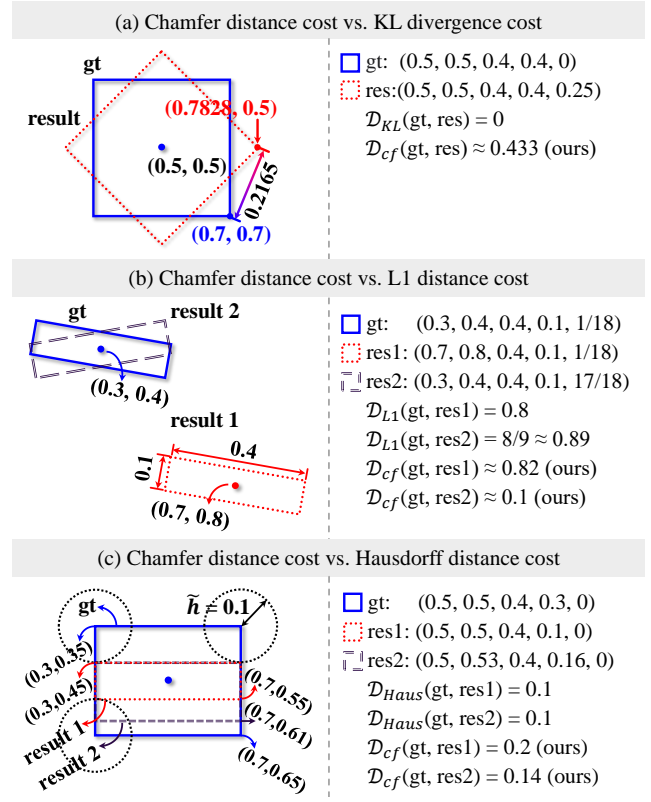


Fig. 9. Comparison of Chamfer distance cost with KL divergence, L1, and Hausdorff distance costs. The centers, sizes, and angles are normalized.

in the Chamfer distance.

Analysis of oriented contrastive denoising. Table X analyzes box noise, angle noise, geometric noise, and probability noise in oriented contrastive denoising. Box noise achieves the best performance, reaching 76.14% AP₅₀ with $\lambda_1 = 1.0$, $\lambda_2 = 2.0$. In contrast, angle noise perturbs only the rotation θ while keeping (c_x, c_y, w, h) unchanged, thus producing a much narrower range of variations. Geometric noise, which combines both box noise and angle noise, tends to generate perturbed boxes that deviate excessively from the ground truth. Since oriented boxes are sensitive to rotation, changes in θ can lead to IoU drops, reducing their effectiveness. Probability noise perturbs the covariance representation of the box, but the induced changes are relatively small and do not effectively influence the box center (c_x, c_y) , resulting in weaker supervision.

When no noise is added, both positive and negative samples are the same as ground-truth boxes. This case leads to two issues. First, the positive samples perfectly match the ground-truth boxes, resulting in zero loss. Second, identical samples are assigned as foreground objects and background at the same time, which confuses the model during training.

Number of denoising query. Table X evaluates the impact of the number of denoising queries. We test a total of 100, 200, and 300 denoising queries, where positive and negative queries are kept in a 1:1 ratio. Increasing the query count from 100 to 200 improves AP₅₀ from 75.83% to 76.14%, while increasing the number to 300 yields nearly a similar result. When the number of denoising queries is small, the randomly generated noised boxes cover only limited cases.

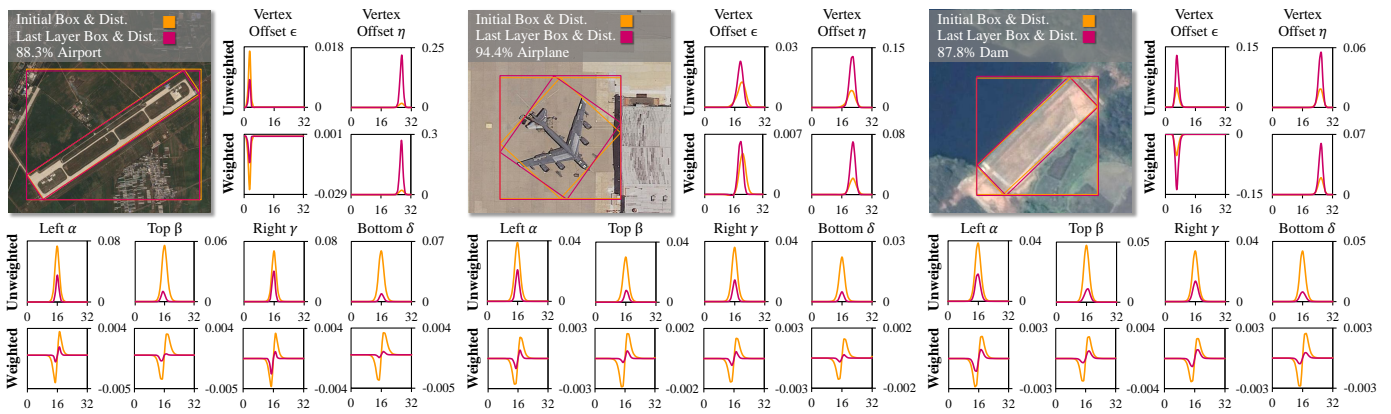


Fig. 10. Analysis of Angle Distribution Refinement, including initial and refined oriented boxes, external rectangles, vertex offsets, with unweighted and weighted distributions.

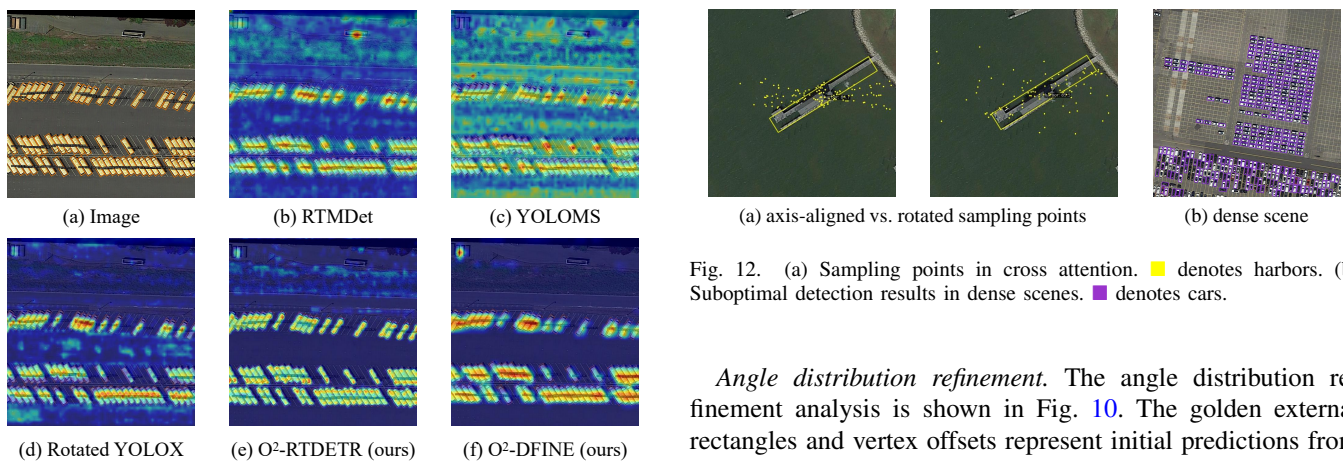


Fig. 11. Visualization of backbone output feature maps. The heatmaps show that our method yields more concentrated and object-aligned activations compared to other methods.

As the number increases, the model benefits from richer noise diversity until it saturates.

E. Qualitative Analysis

Oriented contrastive denoising. Fig. 8 illustrates examples of oriented contrastive denoising under different noise types. The figure includes a box noise example with $\lambda_1 = 1.0$ and $\lambda_2 = 2.0$, an angle noise example with $\lambda_3 = 9.0$ and $\lambda_4 = 18.0$, a geometric noise example combining box and angle perturbations with $\lambda_1 = 1.0$, $\lambda_2 = 2.0$, $\lambda_3 = 9.0$, $\lambda_4 = 18.0$, and a probability noise example with $\lambda_5 = 0.3$ and $\lambda_6 = 0.6$. This provides intuitive insight into how different noise formulations perturb oriented boxes during training.

Chamfer distance cost vs. other costs. Fig. 9 displays examples comparing the Chamfer distance cost with KL divergence, L1, and Hausdorff distance costs. The KL divergence cost is zero when two squares have the same size and center. The L1 distance cost assigns a box far from the ground truth rather than a nearby box. The Hausdorff distance cost is determined by the farthest distance between two point sets. Our Chamfer distance cost effectively overcomes these limitations.

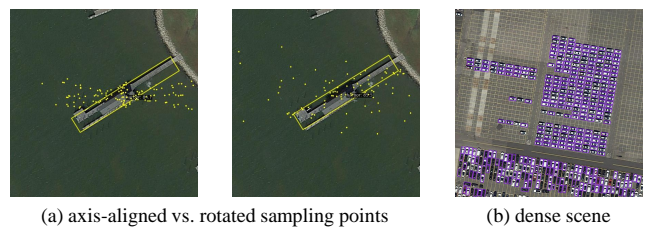


Fig. 12. (a) Sampling points in cross attention. \blacksquare denotes harbors. (b) Suboptimal detection results in dense scenes. \blacksquare denotes cars.

Angle distribution refinement. The angle distribution refinement analysis is shown in Fig. 10. The golden external rectangles and vertex offsets represent initial predictions from the first decoder layer, while the red ones denote refined predictions from the final layer. The golden curves represent the initial unweighted and weighted probability distributions for the vertex offsets (ϵ, η) and the external rectangle edges ($\alpha, \beta, \gamma, \delta$), while the red curves represent the refined distributions. In contrast to DFL [3] without progressive angle refinement, our approach captures this process explicitly. The initial boxes roughly locate the target objects, and the refined distribution further fine-tunes the localization.

Feature response analysis. Fig. 11 visualizes the backbone output feature maps using heatmaps. Compared with other methods, our method produces more compact and discriminative feature responses that align better with object regions. High activations concentrate on object areas, while background responses are suppressed. This demonstrates an improved geometry-aware feature representation for oriented detection.

Sampling points in cross attention. In vanilla cross attention, sampling points are axis-aligned and do not follow object orientation, leading to attention regions misaligned with object boundaries, as shown in Fig. 12(a). In contrast, our method rotates sampling points according to object angles, allowing them to better align with oriented objects.

Result comparison with other detectors. Fig. 13 illustrates a qualitative comparison between our approach and existing detectors on the DOTA-v1.0 dataset across challenging scenarios, including large-scale objects, dense object distributions, and low-light imagery. Our method outperforms other approaches

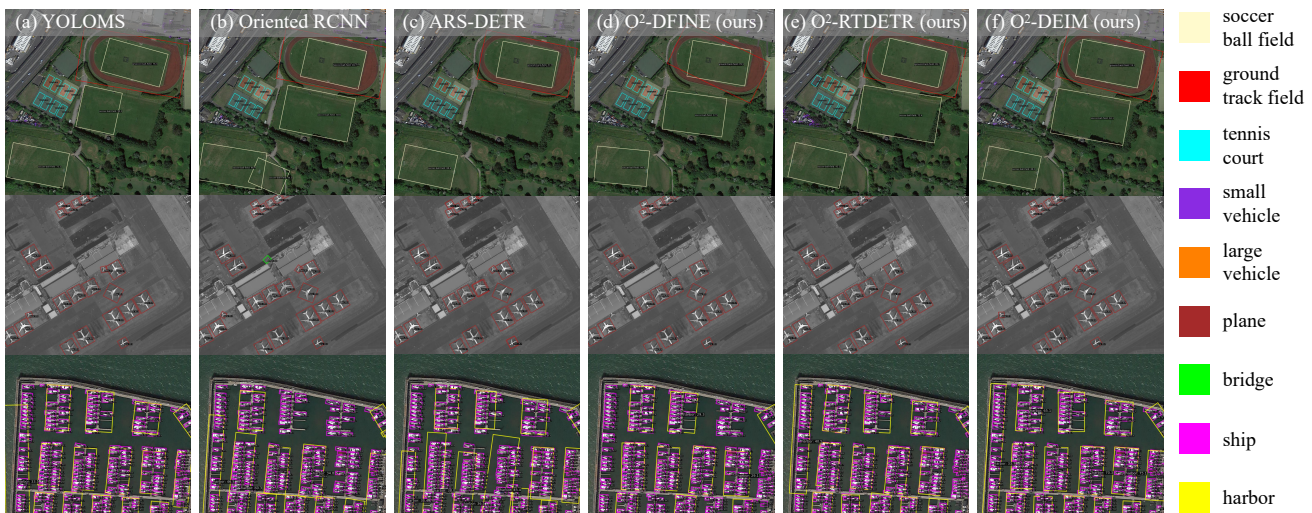


Fig. 13. Qualitative comparison between our method and other detectors on challenging scenarios, including large-scale objects (1st row), low-light conditions (2nd row), and densely distributed objects (3rd row). The confidence threshold is set to 0.3

on large objects, low-light scenes, and dense object layouts, yielding more accurate and stable results. Fig. 12(b) shows suboptimal detection results in dense scenes. Since detection transformers use a fixed number of queries, missed detections occur when the number of objects exceeds the query count.

VI. CONCLUSION

In this paper, we present the first real-time end-to-end oriented object detection transformer for remote sensing images. We first proposed Angle Distribution Refinement, which reformulates angle regression as an iterative refinement of probability distributions to capture rotation uncertainty. To mitigate geometric ambiguity during label assignment, we further introduced the Chamfer distance matching cost. In addition, we designed Oriented Contrastive Denoising with four noise modes to stabilize training, and proposed an instability metric to analyze assignment consistency across decoder layers. Based on these designs, we developed a family of real-time oriented detectors, including O^2 -RTDETR, O^2 -DFINE, and O^2 -DEIM. Extensive experiments on four remote sensing benchmarks demonstrate that our approach achieves a favorable balance between accuracy and speed. Code is available at <https://github.com/wokaikaixin/ai4rs>.

APPENDIX

Rotation-Aware Cross-Attention. In O^2 -RTDETR and O^2 -DEIM cross-attention, the sampling points are rotated around the box center according to the predicted box angle. In D-FINE [14], the cross-attention performs uneven sampling across multiple feature scales. We extend this idea by rotating these unevenly sampled points according to the box orientation, forming the cross-attention used in O^2 -DFINE.

Sampling points in cross-attention. Fig. 14 visualizes the sampling points in cross-attention. In Rotated Deformable DETR, sampling points are axis-aligned and do not follow object orientation, leading to misaligned attention regions. In contrast, O^2 -RTDETR and O^2 -DFINE rotate sampling points

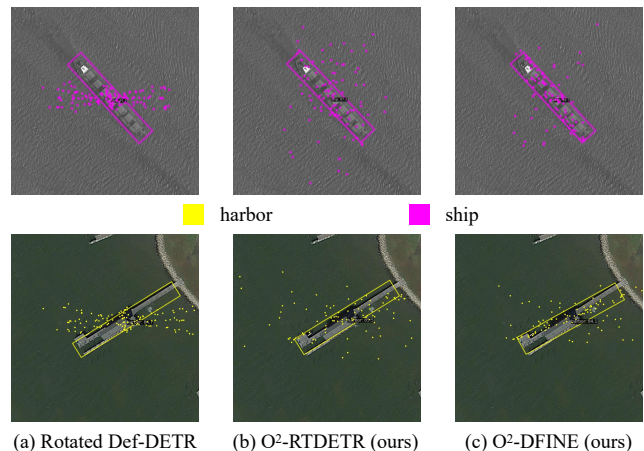


Fig. 14. Visualization of sampling points in cross attention (a) Sampling points in Rotated Deformable DETR. (b) Rotated sampling points in O^2 -RTDETR. (c) Rotated uneven sampling points in O^2 -DFINE.

according to object angles. This allows sampling points to better align with oriented objects.

REFERENCES

- [1] X. Xie, G. Cheng, J. Wang, K. Li, X. Yao, and J. Han, "Oriented r-cnn and beyond," *International Journal of Computer Vision*, vol. 132, no. 7, pp. 2420–2442, 2024.
- [2] C. Lyu, W. Zhang, H. Huang, Y. Zhou, Y. Wang, Y. Liu, S. Zhang, and K. Chen, "Rtmdet: An empirical study of designing real-time object detectors," *arXiv preprint arXiv:2212.07784*, 2022.
- [3] X. Wang, G. Wang, Q. Dang, Y. Liu, X. Hu, and D. Yu, "Pp-yoloe-r: An efficient anchor-free rotated object detector," *arXiv preprint arXiv:2211.02386*, 2022.
- [4] Y. Chen, X. Yuan, J. Wang, R. Wu, X. Li, Q. Hou, and M.-M. Cheng, "Yolo-ms: Rethinking multi-scale representation learning for real-time object detection," *IEEE Transactions on Pattern Analysis and Machine Intelligence*, 2025.
- [5] J. Hosang, R. Benenson, and B. Schiele, "Learning non-maximum suppression," in *Proceedings of the IEEE conference on computer vision and pattern recognition*, 2017, pp. 4507–4515.

- [6] N. Carion, F. Massa, G. Synnaeve, N. Usunier, A. Kirillov, and S. Zagoruyko, "End-to-end object detection with transformers," in *European conference on computer vision*. Springer, 2020, pp. 213–229.
- [7] Z. Zhao, Q. Xue, Y. He, Y. Bai, X. Wei, and Y. Gong, "Projecting points to axes: Oriented object detection via point-axis representation," in *European Conference on Computer Vision*. Springer, 2024, pp. 161–179.
- [8] Y. Zeng, Y. Chen, X. Yang, Q. Li, and J. Yan, "Ars-detr: Aspect ratio-sensitive detection transformer for aerial oriented object detection," *IEEE Transactions on Geoscience and Remote Sensing*, vol. 62, pp. 1–15, 2024.
- [9] J. Zhao, Z. Ding, Y. Zhou, H. Zhu, W.-L. Du, R. Yao, and A. El Saddik, "Rqformer: Rotated query transformer for end-to-end oriented object detection," *Expert Systems with Applications*, vol. 266, p. 126034, 2025.
- [10] H. Lee, M. Song, J. Koo, and J. Seo, "Hausdorff distance matching with adaptive query denoising for rotated detection transformer," in *2025 IEEE/CVF Winter Conference on Applications of Computer Vision (WACV)*. IEEE, 2025, pp. 1872–1882.
- [11] Y. Zhao, W. Lv, S. Xu, J. Wei, G. Wang, Q. Dang, Y. Liu, and J. Chen, "Detrs beat yolos on real-time object detection," in *Proceedings of the IEEE/CVF conference on computer vision and pattern recognition*, 2024, pp. 16965–16974.
- [12] W. Lv, Y. Zhao, Q. Chang, K. Huang, G. Wang, and Y. Liu, "Rt-detr2: Improved baseline with bag-of-freebies for real-time detection transformer," *arXiv preprint arXiv:2407.17140*, 2024.
- [13] S. Wang, C. Xia, F. Lv, and Y. Shi, "Rt-detr3: Real-time end-to-end object detection with hierarchical dense positive supervision," in *2025 IEEE/CVF Winter Conference on Applications of Computer Vision (WACV)*. IEEE, 2025, pp. 1628–1636.
- [14] Y. Peng, H. Li, P. Wu, Y. Zhang, X. Sun, and F. Wu, "D-fine: Redefine regression task of detrs as fine-grained distribution refinement," in *The Thirteenth International Conference on Learning Representations*, 2025.
- [15] S. Huang, Z. Lu, X. Cun, Y. Yu, X. Zhou, and X. Shen, "Deim: Detr with improved matching for fast convergence," in *Proceedings of the Computer Vision and Pattern Recognition Conference*, 2025, pp. 15 162–15 171.
- [16] X. Yang, X. Yang, J. Yang, Q. Ming, W. Wang, Q. Tian, and J. Yan, "Learning high-precision bounding box for rotated object detection via kullback-leibler divergence," *Advances in Neural Information Processing Systems*, vol. 34, pp. 18 381–18 394, 2021.
- [17] E. M. Fenoaltea, I. B. Baybusinov, J. Zhao, L. Zhou, and Y.-C. Zhang, "The stable marriage problem: An interdisciplinary review from the physicist's perspective," *Physics Reports*, vol. 917, pp. 1–79, 2021.
- [18] J. Han, J. Ding, N. Xue, and G.-S. Xia, "Redet: A rotation-equivariant detector for aerial object detection," in *Proceedings of the IEEE/CVF Conference on Computer Vision and Pattern Recognition*, 2021, pp. 2786–2795.
- [19] X. Wu, X. Wang, X. Zhu, L. Yang, J. Liu, and X. Hu, "Measuring the impact of rotation equivariance on aerial object detection," in *Proceedings of the IEEE/CVF International Conference on Computer Vision*, 2025, pp. 7329–7339.
- [20] C. Xu, J. Ding, J. Wang, W. Yang, H. Yu, L. Yu, and G.-S. Xia, "Dynamic coarse-to-fine learning for oriented tiny object detection," in *Proceedings of the IEEE/CVF Conference on Computer Vision and Pattern Recognition*, 2023, pp. 7318–7328.
- [21] Z. Ding, J. Zhao, Y. Zhou, W.-L. Du, H. Zhu, and R. Yao, "Gsdet: Gaussian splatting for oriented object detection," in *Proceedings of the Thirty-Fourth International Joint Conference on Artificial Intelligence, IJCAI-25*, 2025, pp. 900–908.
- [22] J. Zhao, Z. Ding, Y. Zhou, H. Zhu, W.-L. Du, and R. Yao, "Rediffdet: Rotation-equivariant diffusion model for oriented object detection," in *Proceedings of the Computer Vision and Pattern Recognition Conference*, 2025, pp. 24 429–24 439.
- [23] X. Qian, Q. Jian, W. Wang, X. Yao, and G. Cheng, "Incorporating multiscale context and task-consistent focal loss into oriented object detection," *IEEE Transactions on Geoscience and Remote Sensing*, vol. 63, pp. 1–11, 2025.
- [24] X. Qian, B. Wu, G. Cheng, X. Yao, W. Wang, and J. Han, "Building a bridge of bounding box regression between oriented and horizontal object detection in remote sensing images," *IEEE Transactions on Geoscience and Remote Sensing*, vol. 61, pp. 1–9, 2023.
- [25] X. Qian, Z. He, W. Wang, W. Yue, X. Yao, and G. Cheng, "Introducing wso-d-sam proposals and heuristic pseudo-fully supervised training strategy for weakly supervised object detection in remote sensing images," *IEEE Transactions on Geoscience and Remote Sensing*, vol. 64, pp. 1–12, 2026.
- [26] H. Zhang, S. Wen, Z. Wei, and Z. Chen, "High-resolution feature generator for small-ship detection in optical remote sensing images," *IEEE Transactions on Geoscience and Remote Sensing*, vol. 62, pp. 1–11, 2024.
- [27] C. Guo, Z. Ma, Y. Zhao, C. Cao, Z. Jiang, and H. Zhang, "Multi-instance mining with dynamic localization for weakly supervised object detection in remote-sensing images," *International Journal of Remote Sensing*, vol. 46, no. 9, pp. 3487–3512, 2025.
- [28] M. Dang, G. Liu, A. W.-K. Kong, Z. Zheng, N. Luo, and R. Pan, "Ro2-detr: Rotation-equivariant oriented object detection transformer with 1d rotated convolution kernel," *ISPRS Journal of Photogrammetry and Remote Sensing*, vol. 228, pp. 166–178, 2025.
- [29] M. Zhang, H. Qiu, L. Wang, H. Cheng, T. Zhao, and H. Li, "Oriented-dino: Angle decoupling prediction and consistency optimizing for oriented detection transformer," *IEEE Transactions on Geoscience and Remote Sensing*, 2024.
- [30] J. Zhao, Z. Ding, Y. Zhou, H. Zhu, W.-L. Du, R. Yao, and A. El Saddik, "Orientedformer: An end-to-end transformer-based oriented object detector in remote sensing images," *IEEE Transactions on Geoscience and Remote Sensing*, 2024.
- [31] Z. Hu, K. Gao, X. Zhang, J. Wang, H. Wang, Z. Yang, C. Li, and W. Li, "Emo2-detr: Efficient-matching oriented object detection with transformers," *IEEE Transactions on Geoscience and Remote Sensing*, 2023.
- [32] J. Redmon, S. Divvala, R. Girshick, and A. Farhadi, "You only look once: Unified, real-time object detection," in *Proceedings of the IEEE conference on computer vision and pattern recognition*, 2016, pp. 779–788.
- [33] C. Li, L. Li, H. Jiang, K. Weng, Y. Geng, L. Li, Z. Ke, Q. Li, M. Cheng, W. Nie *et al.*, "Yolov6: A single-stage object detection framework for industrial applications," *arXiv preprint arXiv:2209.02976*, 2022.
- [34] R. Varghese and S. M., "Yolov8: A novel object detection algorithm with enhanced performance and robustness," in *2024 International Conference on Advances in Data Engineering and Intelligent Computing Systems (ADICS)*, 2024, pp. 1–6.
- [35] C.-Y. Wang, I.-H. Yeh, and H.-Y. Mark Liao, "Yolov9: Learning what you want to learn using programmable gradient information," in *European conference on computer vision*. Springer, 2024, pp. 1–21.
- [36] Y. Tian, Q. Ye, and D. Doermann, "Yolov12: Attention-centric real-time object detectors," *Advances in neural information processing systems*, 2025.
- [37] Z. Ge, S. Liu, F. Wang, Z. Li, and J. Sun, "Yolox: Exceeding yolo series in 2021," *arXiv preprint arXiv:2107.08430*, 2021.
- [38] R. Khanam and M. Hussain, "What is yolov5: A deep look into the internal features of the popular object detector," *arXiv preprint arXiv:2407.20892*, 2024.
- [39] T. He, Z. Zhang, H. Zhang, Z. Zhang, J. Xie, and M. Li, "Bag of tricks for image classification with convolutional neural networks," in *Proceedings of the IEEE/CVF conference on computer vision and pattern recognition*, 2019, pp. 558–567.
- [40] Y. Ma, D. Yu, T. Wu, and H. Wang, "Paddlepaddle: An open-source deep learning platform from industrial practice," *Frontiers of Data and Computing*, vol. 1, no. 1, pp. 105–115, 2019.
- [41] G.-S. Xia, X. Bai, J. Ding, Z. Zhu, S. Belongie, J. Luo, M. Datcu, M. Pelillo, and L. Zhang, "Dota: A large-scale dataset for object detection in aerial images," in *Proceedings of the IEEE conference on computer vision and pattern recognition*, 2018, pp. 3974–3983.
- [42] G. Cheng, J. Wang, K. Li, X. Xie, C. Lang, Y. Yao, and J. Han, "Anchor-free oriented proposal generator for object detection," *IEEE Transactions on Geoscience and Remote Sensing*, vol. 60, pp. 1–11, 2022.
- [43] X. Sun, P. Wang, Z. Yan, F. Xu, R. Wang, W. Diao, J. Chen, J. Li, Y. Feng, T. Xu, M. Weinmann, S. Hinz, C. Wang, and K. Fu, "Fair1m: A benchmark dataset for fine-grained object recognition in high-resolution remote sensing imagery," *ISPRS Journal of Photogrammetry and Remote Sensing*, vol. 184, pp. 116–130, 2022.
- [44] C. Lee, J. Son, H. Shon, Y. Jeon, and J. Kim, "Fred: Towards a full rotation-equivariance in aerial image object detection," in *Proceedings of the AAAI Conference on Artificial Intelligence*, vol. 38, no. 4, 2024, pp. 2883–2891.
- [45] J. H. L. Marques, J. Murrugarra-Llerena, and C. R. Jung, "Gaucho: Gaussian distributions with cholesky decomposition for oriented object detection," in *Proceedings of the Computer Vision and Pattern Recognition Conference*, 2025, pp. 3593–3602.
- [46] H. Xu, X. Liu, H. Xu, Y. Ma, Z. Zhu, C. Yan, and F. Dai, "Rethinking boundary discontinuity problem for oriented object detection," in *Proceedings of the IEEE/CVF Conference on Computer Vision and Pattern Recognition*, 2024, pp. 17 406–17 415.

- [47] X. Cai, Q. Lai, Y. Wang, W. Wang, Z. Sun, and Y. Yao, "Poly kernel inception network for remote sensing detection," in *Proceedings of the IEEE/CVF conference on computer vision and pattern recognition*, 2024, pp. 27 706–27 716.
- [48] Y. Li, Q. Hou, Z. Zheng, M.-M. Cheng, J. Yang, and X. Li, "Large selective kernel network for remote sensing object detection," in *Proceedings of the IEEE/CVF International Conference on Computer Vision (ICCV)*, October 2023, pp. 16 794–16 805.
- [49] Y. Yu and F. Da, "Phase-shifting coder: Predicting accurate orientation in oriented object detection," in *Proceedings of the IEEE/CVF Conference on Computer Vision and Pattern Recognition*, 2023, pp. 13 354–13 363.
- [50] J. Ding, N. Xue, Y. Long, G.-S. Xia, and Q. Lu, "Learning roi transformer for oriented object detection in aerial images," in *Proceedings of the IEEE/CVF Conference on Computer Vision and Pattern Recognition*, 2019, pp. 2849–2858.
- [51] W. Li, Y. Chen, K. Hu, and J. Zhu, "Oriented reppoints for aerial object detection," in *Proceedings of the IEEE/CVF conference on computer vision and pattern recognition*, 2022, pp. 1829–1838.
- [52] T.-Y. Lin, P. Goyal, R. Girshick, K. He, and P. Dollár, "Focal loss for dense object detection," in *Proceedings of the IEEE international conference on computer vision*, 2017, pp. 2980–2988.
- [53] Z. Cai and N. Vasconcelos, "Cascade r-cnn: Delving into high quality object detection," in *Proceedings of the IEEE conference on computer vision and pattern recognition*, 2018, pp. 6154–6162.
- [54] S. Ren, K. He, R. Girshick, and J. Sun, "Faster r-cnn: Towards real-time object detection with region proposal networks," *Advances in neural information processing systems*, vol. 28, 2015.